The Astrophysical Journal Supplement Series, 138:315–336, 2002 February

THE BOOMERANG NORTH AMERICA INSTRUMENT: A BALLOON-BORNE BOLOMETRIC RADIOMETER OPTIMIZED FOR MEASUREMENTS OF COSMIC BACKGROUND RADIATION ANISOTROPIES FROM 0°.3 TO 4°

F. Piacentini,[1] P. A. R. Ade,[2] R. S. Bhatia,[3] J. J. Bock,[3,4] A. Boscaleri,[5] P. Cardoni,[6] B. P. Crill,[3] P. de Bernardis,[1] H. Del Castillo,[4] G. De Troia,[1] P. Farese,[1] M. Giacometti,[1] E. F. Hivon,[3] V. V. Hristov,[3] A. Iacoangeli,[1] A. E. Lange,[3] S. Masi,[1] P. D. Mauskopf,[3,7] L. Miglio,[1,8] C. B. Netterfield,[3,8] P. Palangio,[9] E. Pascale,[3,5] A. Raccanelli,[1] S. Rao,[1,9] G. Romeo,[9] J. Ruhl,[10] and F. Scaramuzzi[6]

Received 2001 May 9; accepted 2001 September 10

ABSTRACT

We describe the BOOMERANG North America instrument, a balloon-borne bolometric radiometer designed to map the cosmic microwave background (CMB) radiation with 0°.3 resolution over a significant portion of the sky. This receiver employs new technologies in bolometers, readout electronics, millimeter-wave optics and filters, cryogenics, scan, and attitude reconstruction. All these subsystems are described in detail in this paper. The system has been fully calibrated in flight using a variety of techniques, which are described and compared. Using this system, we have obtained a measurement of the first peak in the CMB angular power spectrum in a single, few hour long balloon flight. The instrument described here was a prototype of the BOOMERANG Long Duration Balloon experiment.

Subject headings: balloons — cosmic microwave background — cosmology: observations — instrumentation: photometers

1. INTRODUCTION

The existence of the 2.7 K cosmic microwave background (CMB) radiation is evidence that our universe originated from a hot, dense plasma (Hu, Sugiyama, & Silk 1997). This radiation was emitted in the early universe, when the plasma cooled enough for protons and electrons to form hydrogen atoms. Before recombination, photons and baryons were tightly coupled by Compton scattering. After recombination the photons and baryons are highly decoupled, with a mean free path longer than the causal horizon. This event is dated ~300,000 yr after the big bang, when the universe was ~1000 times smaller and ~50,000 times younger (redshift $z = 1000$). The properties of the CMB reflect the conditions of the early universe and are closely linked with global properties of the universe, such as the energy density ($\Omega_{\rm tot}$), composition (Ω_b, Ω_Λ, $\Omega_{\rm DM}$), and expansion rate (H_0).

In particular, variations in the brightness of the CMB, or anisotropies, reflect variations in temperature, density, and velocity of the last scattering surface. These fluctuations, which originated from random noise at an earlier phase of expansion, are the seeds for the formation of structures such as galaxies and clusters of galaxies present in the universe today. Precise measurements of the angular power spectrum of CMB anisotropies (White, Scott, & Silk 1994) can discriminate between competing cosmological models and, if the inflationary scenario is correct, accurately determine many of the physical parameters of the universe.

The *COBE*-DMR detection (Smoot et al. 1991, 1992) of anisotropies in the CMB at large angular scales provides a point of reference for theoretical models of the origin of fluctuations in the CMB (Bond et al. 1994). Measurements at smaller angular scales are needed to fully understand the nature of these fluctuations. Since the launching of *COBE*, many other experiments have made significant detections of CMB anisotropy at a wide variety of angular scales, from 0°.3 to 10°. The latest results in measurements of the angular power spectrum of the CMB anisotropies and cosmological parameters extraction are in de Bernardis et al. (2000, 2002), Lange et al. (2001), Jaffe et al. (2001), Pryke et al. (2002), and Netterfied et al. (2002).

The new generation of CMB experiments is designed to probe models of structure formation with a combination of higher sensitivity, sky coverage, and resolving power. Advances in detector technology have resulted in radiometers that are over 100 times more sensitive than the *COBE*-DMR per unit time. In addition, improved techniques for removing noise from atmospheric fluctuations with both single-dish instruments and interferometers allow increased sensitivity with ground-based telescopes. Long-duration balloon (LDB) platforms provide the opportunity to obtain the long integration times needed for large sky coverage with balloon-borne telescopes.

BOOMERANG is an experiment designed to measure the detailed structure of the CMB at angular scales from 0°.2 to 4° with high sensitivity. The BOOMERANG instrument consists of a 1.3 m balloon-borne telescope and pointing platform with a 300 mK bolometric array receiver. The receiver is contained inside a liquid nitrogen (LN_2) and liquid helium (LHe) cryostat with a hold time of 2 weeks.

[1] Dipartimento di Fisica, Universitá La Sapienza, Piazzale Aldo Moro 2, 00185 Roma, Italy; francesco.piacentini@roma1.infn.it.
[2] Department of Physics, Queen Mary and Westfield College, Mile End Road, London E1 4NS, UK.
[3] Department of Physics, Math, and Astronomy, California Institute of Technology, 1201 East California Boulevard, Pasadena, CA 91125.
[4] Jet Propulsion Laboratory, 4800 Oak Grove Drive, Pasadena, CA 91109.
[5] IROE-CNR, Via Panciatichi 54, 50127 Firenze, Italy.
[6] Ente Nazionale Energie Alternative, Via Enrico Fermi 45, 00044 Frascati, Italy.
[7] Department of Physics and Astronomy, University of Wales, 5, The Parade, Cardiff CF24 3YB, UK.
[8] Department of Astronomy, University of Toronto, 60 St. George Street, ON M5S 3H8, Canada.
[9] Istituto Nazionale di Geofisica, Via di Vigna Murata, 605, 00143 Roma, Italy.
[10] Department of Physics, University of California, Santa Barbara, CA.

The measurement technique consists of measuring a sky brightness map by slowly scanning the telescope (and the full payload) in azimuth, using the Earth rotation to cover a wide sky region. There is no mechanical chopper. The scan converts CMB anisotropies at different angular scales into detector signals at different subaudio frequencies. The instrument features a new total power readout of the detectors, optimized to preserve the information content of the signal while rejecting very low and very high frequency noise. This approach pioneers in several aspects the HFI instrument on the *Planck* satellite.

In this paper we describe the instrument prototype as it was used for the test flight, on 1997 August 30, to qualify all the flight subsystems for later use in the Antarctic LDB flight. During the 1997 test flight we observed about 200 deg^2 of sky at high Galactic latitudes. Science results from that flight are reported in Mauskopf et al. (2000) and Melchiorri et al. (2000). Here we give all the technical details of the instrument as well as its performance during the test flight: thermal performance, bolometer loading and noise, scan performance, attitude reconstruction, and calibration on Jupiter and on the CMB dipole. The LDB instrument is described in B. P. Crill et al. (2002, in preparation).

2. INSTRUMENT

BOOMERANG is designed to take advantage of the long integration time possible from a balloon-borne platform flown over the Antarctic. Antarctic summer ballooning is very attractive for CMB anisotropy experiments for two reasons. The first is that the flight duration (up to ~20 days) allows for substantial sky coverage and deep checks for systematics; the second is that very low foreground regions are observable in the direction generally opposite the Sun during the Antarctic summer.

There are, however, a number of challenges peculiar to Antarctic ballooning. The long flight duration requires special cryogenic systems. The cosmic-ray flux in polar regions is enhanced by a factor of about 10 with respect to North American latitudes, thus resulting in a high noise in standard bolometric detectors. The continual presence of the Sun during an Antarctic LDB flight is a general concern for the thermal performance of the payload and for pickup in the sidelobes of the telescope. The balloon is far from the ground equipment, so special data collection and telemetry systems have to be used, and interactivity with the system is reduced.

We describe in the following the solutions we have adopted to overcome these problems, developing custom subsystems: a long-duration cryostat, spider web bolometers, low sidelobes off-axis optics, special Sun shields and telescope baffling, and total power readout.

A general view of the experiment with its main subsystems is shown in Figure 1.

2.1. *Optics*

The BOOMERANG telescope consists of an ambient temperature 1.3 m diameter off-axis parabolic primary mir-

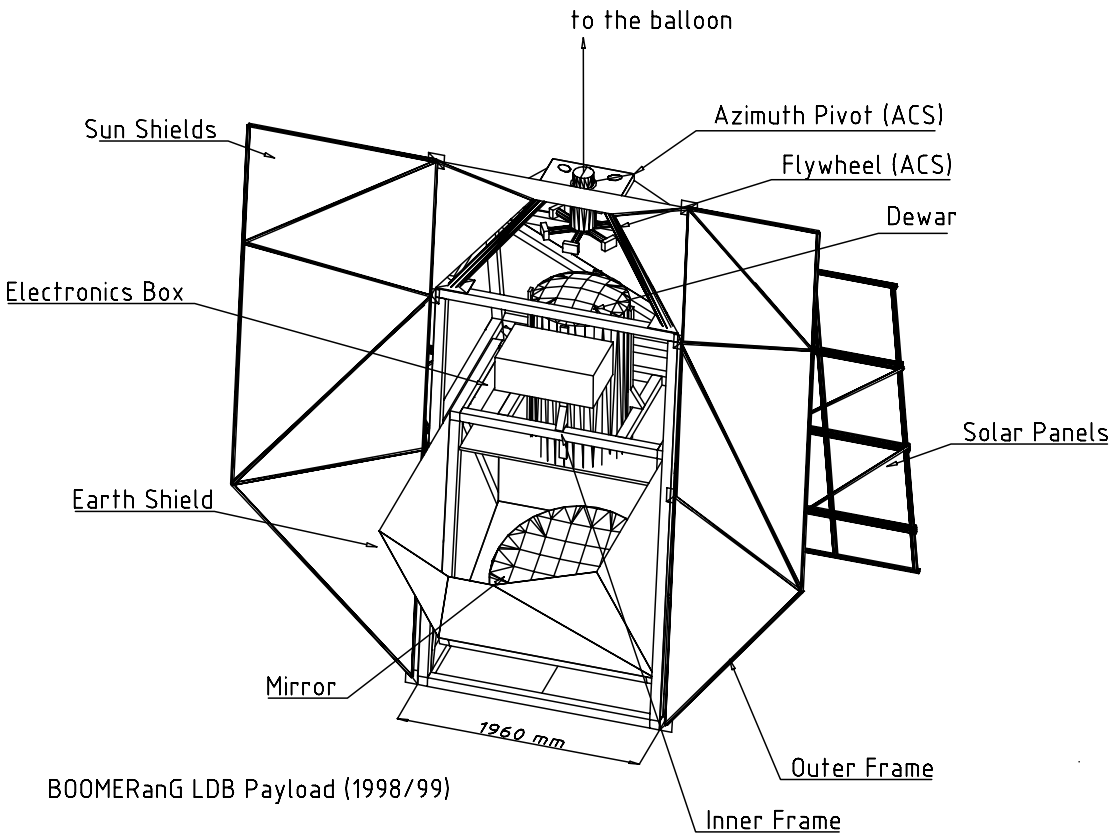

FIG. 1.—BOOMERANG payload. Special shields in aluminized Mylar protect from Sun and Earth radiation. Radiation coming from the sky is reflected into the cryostat by means of the 1.3 m primary mirror. Solar panels are used for power supply in the LDB flight, while lithium batteries were used in the BNA flight. The attitude contol system provides pointing and scanning of the telescope.

ror ($f = 1280$ mm, 45° off-axis) that feeds cold reimaging secondary and tertiary mirrors inside a large liquid helium cryostat. The telescope and the cryostat are both mounted on an aluminum frame (the inner frame of the payload), which can be tipped in elevation by $-12°$ to $+20°$ to cover elevation angles from 33° to 65°. The primary mirror has a 45° off-axis angle. Radiation from the sky is reflected by the primary mirror and enters the cryostat through a thin (50 μm) polypropylene window near the prime focus. Two circular windows side by side, each 66 mm in diameter, are used. This geometry provides a wide field of view while allowing the use of thin window material, which minimizes the emission from this ambient temperature surface. Filters rejecting high-frequency radiation are mounted on the 77 and 2 K shields in front of the cold reimaging optics. Fast off-axis secondary and tertiary mirrors surrounded by absorbing baffles reimage the prime focus onto the detector focal plane.

The BOOMERANG optics (Fig. 2) is optimized for an array with widely separated pixels. The advantage of having large spacing between pixels in the focal plane is the ability to difference (or compare) the signals from two such pixels and remove correlated optical fluctuations such as temperature drift of the telescope, while retaining high sensitivity to structure on the sky at angles up to the pixel separation. This scheme eliminates the need for moving optical compo-

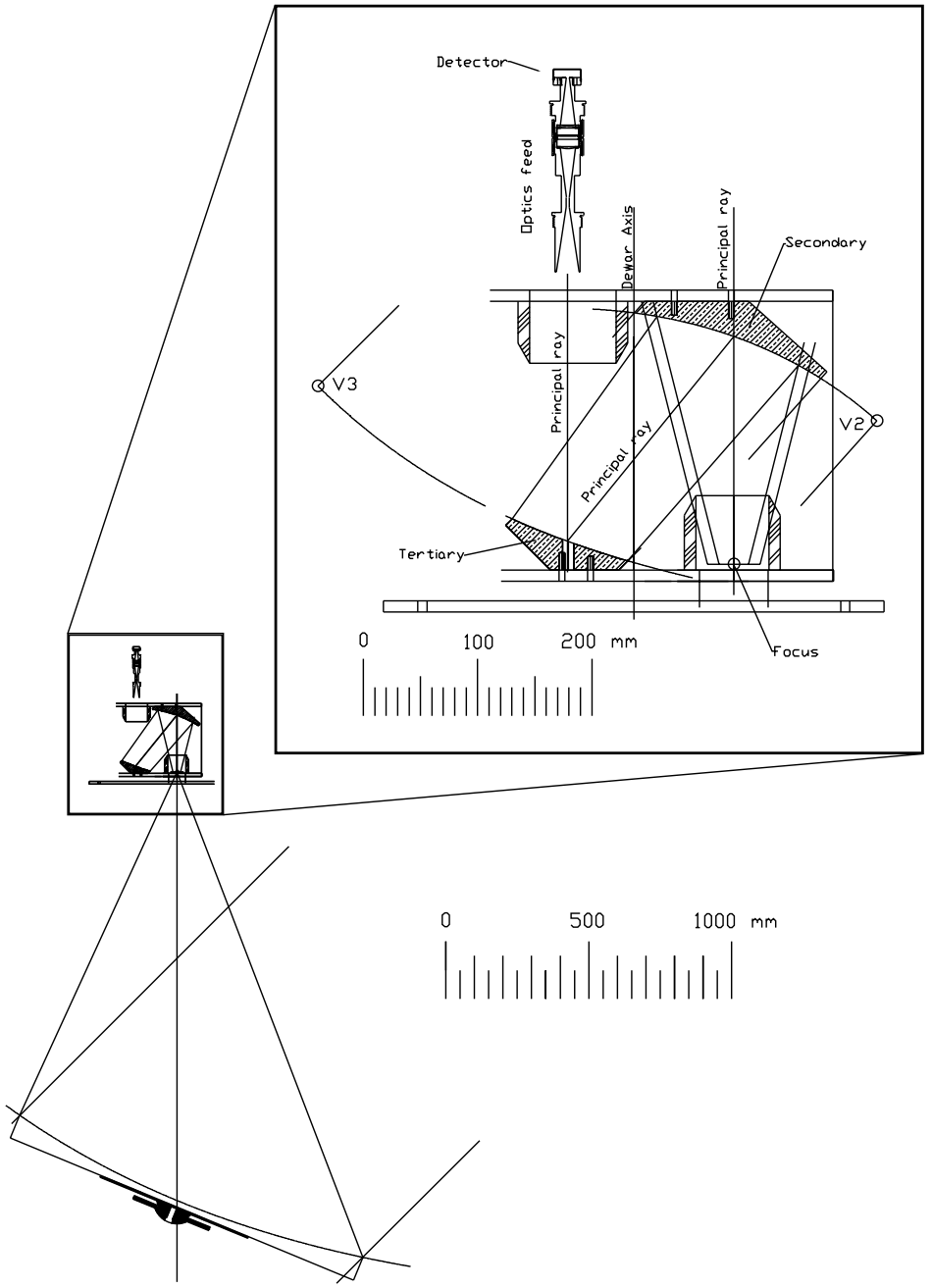

FIG. 2.—BOOMERANG optics. Secondary and tertiary mirrors project the image on the focal plane, where the feed horns concentrate the radiation on the detectors. They are cooled to 2 K inside the main cryostat. An image of the 1.3 m primary mirror is formed on the tertiary mirror, which works as a cold Lyot stop, improving the off-axis rejection of the photometer.

TABLE 1
IDEAL PARAMETERS FOR THE EQUATION OF THE THREE BOOMERANG MIRRORS[a]

Mirror	R (mm)	k	A (mm^{-3})	B (mm^{-5})
Primary.....	2560	−1.0	0.0	0.0
Secondary...	363.83041	−0.882787413818	1.3641139×10^{-9}	$1.8691461 \times 10^{-15}$
Tertiary.....	545.745477407	−1.0	$4.3908607 \times 10^{-10}$	$-3.2605391 \times 10^{-15}$

[a] See eq. [1].

nents and simplifies the design and operation of the experiment.

We optimized the optics for diffraction-limited performance at 1 mm over a $2^\circ \times 5^\circ$ field of view. The reimaging optics are configured to form an image of the primary mirror at the 10 cm diameter tertiary mirror. The size of the tertiary mirror therefore limits the illumination pattern on the primary mirror, which is underfilled by 50% in area (85 cm in diameter) to improve sidelobe rejection.

The secondary mirror is an ellipsoid, and the tertiary is a paraboloid, 10 cm in diameter, corresponding to an 85 cm diameter aperture on the 1.3 m primary mirror. The equation describing the three mirrors is

$$z(r) = \frac{r^2}{R\left[1 + \sqrt{1 - (1+k)(r^2/R^2)}\right]} + Ar^4 + Br^6 , \quad (1)$$

with parameters R, k, A, and B as in Table 1.

The BOOMERANG North America (BNA) focal plane contains single-frequency channels fed by conical or Winston horns. Although the image quality from the optics is diffraction limited over a $2^\circ \times 5^\circ$ field, all of the feed optics are placed inside two circles 2° in diameter, separated by $3^\circ.5$ center to center. The focal plane area outside these circles is vignetted by blocking filters at the entrance to the optics box and on the 77 K shield and is unusable. Because of the curvature of the focal plane, the horns are placed at the positions of the beam centroids determined by geometric ray tracing. All of the feeds are oriented toward the center of the tertiary mirror. The configuration of the focal plane for the North American flight is in Figure 3.

The BNA frequency bands are centered at 90 and 150 GHz and are optimized to maximize sensitivity to CMB fluctuations, identify dust emission, and reject radiation from atmospheric line emission. The low-pass filters mounted on the 77 and 2 K optical entrance windows provide good transmission across these bands while effectively blocking higher frequency radiation. Two metal mesh low-pass filters with cutoff frequencies of 480 GHz are mounted on the 77 K stage. The filters are 65 mm in diameter, and each one is directly behind one of the 50 μm polypropylene vacuum windows. Two more low-pass filters with a cutoff frequency of 300 GHz are mounted on the 2 K stage at the entrance to the cold optics box. Although each filter has a leak at twice the cutoff frequency, the combination eliminates these leaks. Because these filters are reflective at frequencies above the cutoff, they minimize the radiation heat load on the cryogens. While the metal mesh filters have high reflectivity at high frequencies, they are not impenetrable, and above a few THz any transmission at the level of less than 10^{-3} is significant. Therefore, we place a dielectric absorber behind the 300 GHz filter on the 2 K stage that has a cutoff frequency of 1650 GHz. The absorber is 0.5 mm thick alkali-halide filter coated with a 130 μm thick layer of black polyethylene. This low-pass filter stack has a trans-

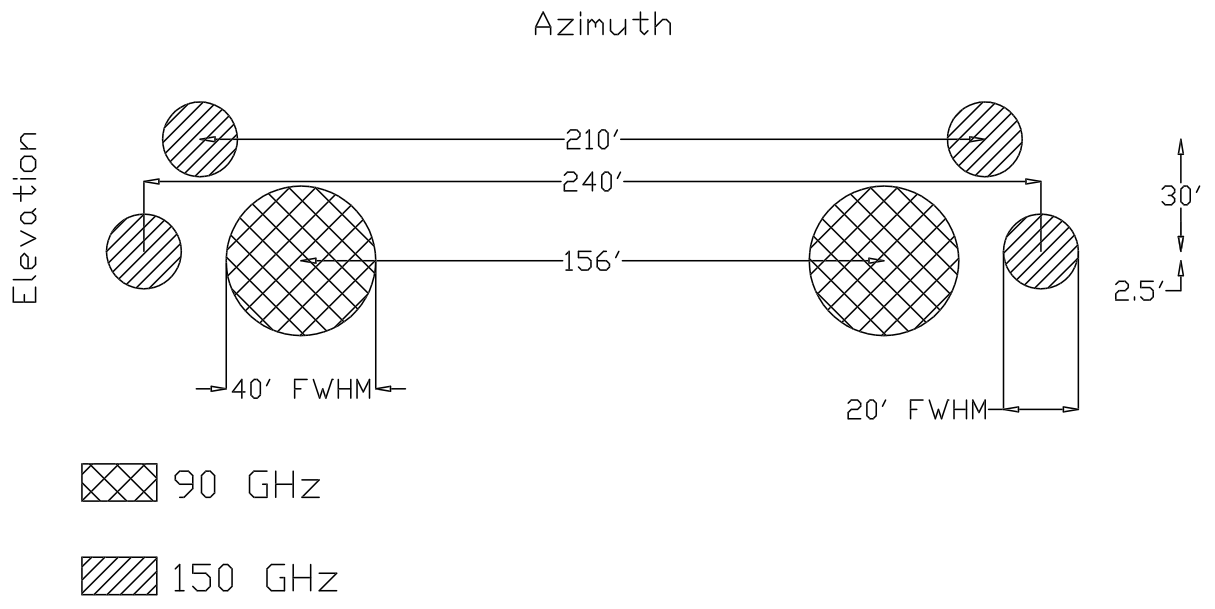

FIG. 3.—Location of the beams in the focal plane of the BNA photometer

mission of greater than 80% at all frequencies from 90 to 410 GHz while attenuating at a level 5×10^{-4} between 1650 GHz and 100 THz and at a level 10^{-3} over 100 THz. All of the other filtering is done in the focal plane elements.

We have produced two different feeds designed to efficiently couple to the telescope and produce beam sizes on the sky of 20′ and 40′. These sizes are larger than the diffraction limit: we traded resolution for throughput to obtain good sensitivity to diffuse radiation even in a short test flight. The design of the single-frequency feed structure is shown in Figure 4 and is similar to the feed design described in Church et al. (1997). This design allows us to illuminate correctly the band-defining filters and create an effective Faraday cage surrounding the bolometric detectors.

Each feed consists of a band-defining filter stack mounted inside waveguide optics that couple the radiation from the tertiary mirror into an integrating bolometer cavity. The feed is divided in two parts separated by a 0.5 mm gap, one held at 2 K and the other at 300 mK.

The entrance horns are mounted in a horn-positioning flange held at 2 K. Each horn couples to a section of waveguide with length 2λ that acts as a high-pass filter and rejects radiation with wavelength $\lambda > 3.41a$, where a is the radius of the waveguide. The 20′ horns have an entrance aperture of 19.7 mm at $f = 3.3$ and a waveguide diameter of 2.54 mm. The throughput is limited by a combination of the entrance aperture of the horns and the size of the Lyot stop to be $A\Omega_{\rm total} = 0.1$ cm^2 sr for the 20′ horns. This value is over the diffraction limit throughput $A\Omega_{\rm horn} \simeq \lambda^2 = 0.04$ cm^2 sr at $\lambda \simeq 2$ mm (150 GHz). The 40′ horns have an entrance aperture of 33 mm and a waveguide diameter of 5.1 mm. These channels have approximately 3 times the

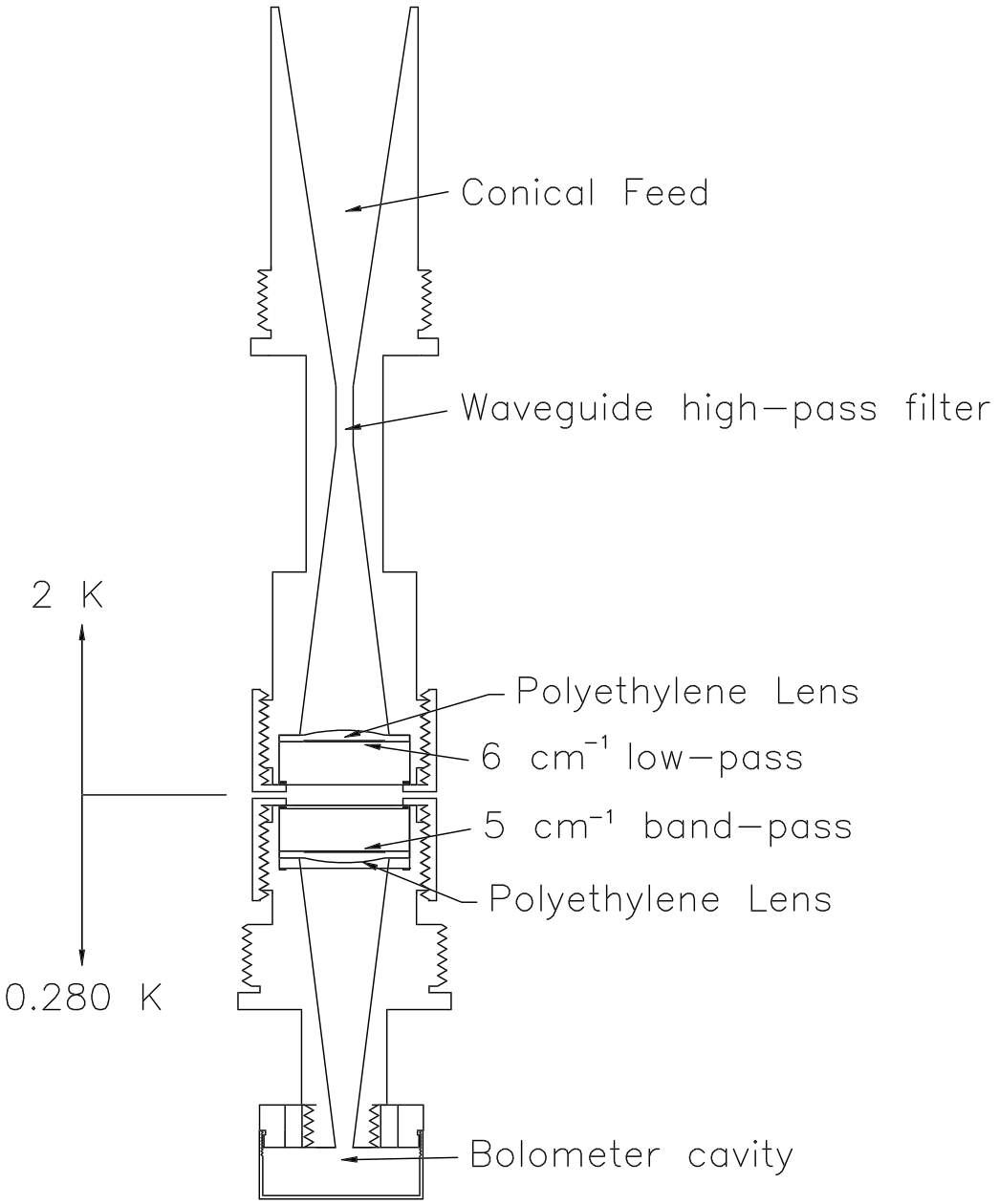

FIG. 4.—150 GHz feed horn. The upper part is cooled at less than 2 K and the lower part to 0.280 K. See text for description.

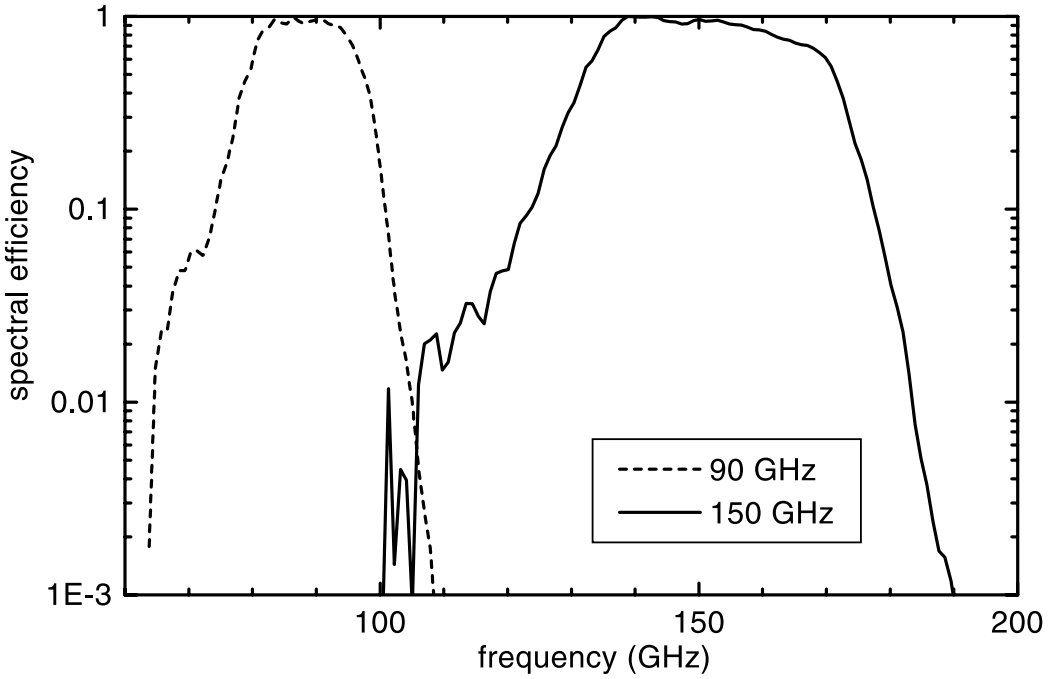

FIG. 5.—Frequency response of a 90 and a 150 GHz channel as measured with a Fourier transform spectrometer

throughput of the 20′ channels with $A\Omega \simeq 0.3$ cm^2 sr, while the diffraction limit is 0.1 cm^2 sr.

On the other side of the waveguide is an f/4 conical horn that expands the waveguide to a diameter of 17.8 mm in the 20′ channel and 27.9 mm in the 40′ channel. At the end of this cone, the feed opens up to allow the mounting of a converging lens and an oversized metal mesh dichroic filter. A bandpass filter followed by another identical converging lens and conical horn are held at 300 mK across the small gap of less than 1 mm. This final horn feeds a small cavity containing a micromesh bolometer, which absorbs more than 90% of the radiation entering the cavity. In the geometrical limit, the lenses reimage to infinity a point at the vertex of the horns on which they are mounted. In the diffraction limit, they each produce a beam waist at the center of the length of waveguide that contains the filters, thereby improving the coupling between the expanding horn at 2 K and the concentrating horn at 300 mK.

The spectral bands are defined by the 300 mK bandpass filters, metal mesh resonant grid filters with nominal central frequencies of 90 and 150 GHz and 30% bandwidth. These filters have high transmission in band with sharp band edges, but their performance degrades quickly as a function of off-axis angle. The f/4 horns in the intermediate section of the feed structure ensure that the filters are illuminated with small off-axis angles. The bandpass filters also have a leak at approximately twice the central frequency. The 2 K dichroic filters in the feed structure eliminate these leaks and provide additional high-frequency blocking with cutoff frequencies of 172 GHz for the 90 GHz channel and 217 GHz for the 150 GHz channel. The frequency response of a 90 and a 150 GHz channel, measured with a Fourier transform spectrometer, are shown in Figure 5. The out-of-band transmission is less than -25 dB for $\nu < 900$ GHz.

We have measured the optical efficiency of this structure equipped with filters for both 90 and 150 GHz operation. The optical efficiency measurements were made using black loads of Eccosorb foam at 77 and 300 K. We measure the difference in optical power on a bolometer by comparing the DC-coupled current-voltage curves of the detector under the different loading conditions. Preflight results are in § 5.

Tables 2 and 3 give the band centroids and widths for the BOOMERANG photometers, along with the estimated loadings from the CMB, the telescope, and the atmosphere.

2.2. *Detectors*

BOOMERANG uses bolometers to detect the fluctuations in incoming radiation. A bolometer consists of a broadband absorber with heat capacity C, that has a weak thermal link G, to a thermal bath at a temperature T_b. Inci-

TABLE 2
BOOMERANG NORTH AMERICA FILTER BANDS

$\nu_{\rm nominal}$ (GHz)	$\nu_{\rm peak}$ (GHz)	$\nu_0^{\rm CMB}$ (GHz)	$\nu_0^{\rm R\text{-}J}$ (GHz)	$\Delta\nu_{\rm FWHM}$ (GHz)
90.....	88.5	93.6	94.1	33
150.....	136.5	155.7	157.9	54

NOTE.—$\nu_{\rm peak}$ is the peak for a flat spectrum; $\nu_0^{\rm CMB}$ and $\nu_0^{\rm R\text{-}J}$ are the peaks for CMB and Rayleigh-Jeans spectra, respectively.

TABLE 3
BOOMERANG/NA IN-FLIGHT EXPECTED LOADINGS

$\nu_{\rm peak}$ (GHz)	$A\Omega$ (cm^2 sr)	$P_{\rm atm}$ (pW)	$P_{\rm CMB}$ (pW)	$P_{\rm tel}$ (pW)
88.5.....	0.3	0.004	0.10	0.42
136.5....	0.1	0.28	0.17	1.6

dent radiation produces a temperature rise in the absorber that is read out with a current-biased thermistor. The sensitivity of a bolometer expressed in noise equivalent power (NEP) is given by

$$\mathrm{NEP}_{\mathrm{bolo}} = \gamma\sqrt{4kT_b^2G}\,, \tag{2}$$

where γ is a constant of order unity that depends weakly on the sensitivity of the thermistor and k is Boltzmann's constant. The dynamical equation for the temperature of the thermistor can be expressed as

$$\frac{dT_{\mathrm{bolo}}}{dt} = \frac{P_{\mathrm{in}} - G(T_{\mathrm{bolo}} - T_b)}{C}\,, \tag{3}$$

where P_{in} is the incident power. From this equation, we can see that bolometers have a finite bandwidth limited by the time for the absorber to come to equilibrium after a change in incident power, $\tau = C/G$. Previous balloon-borne bolometric receivers have been limited in sensitivity or bandwidth by the properties of the materials used for fabrication of the detectors.

Bolometers are also limited in sensitivity by external sources of noise such as cosmic rays, microphonic disturbances, and radio frequency interference (RFI). Of particular importance for BOOMERANG is the cosmic-ray rate on the Antarctic stratosphere, which is about 1 order of magnitude higher than at North American latitudes because the magnetic field of the Earth funnels charged particles to the poles. We have experience of cosmic-ray hits from many bolometric receivers flown at balloon altitude at temperate latitudes. The cosmic-ray hit rate for the MAX experiment (Alsop et al. 1992) during a North American balloon flight was 0.14 Hz. In order to remove spurious signals from these cosmic-ray interactions, cosmic rays were identified and a length of data corresponding to 10 detector time constants was removed. Because the MAX detector time constants were all less than 30 ms, this resulted in a loss of 5% of the data, which did not severely affect the sensitivity. Almost one-half of the data would be contaminated by cosmic rays with the same detectors operated from an LDB over the Antarctic.

In the North American flight of BOOMERANG we tested for the first time bolometers with a new architecture, consisting of a micromesh absorber with an indium bump-bonded neutron transmutation doped (NTD) germanium thermistor. These bolometers can have lower heat capacity, lower thermal conductivities, lower cosmic-ray cross section, and less sensitivity to microphonic heating than previous 300 mK bolometers. The micromesh absorbers and support structures are fabricated from a thin film of silicon nitride using microlithography. The absorber is a circular grid with 60–400 μm grid spacing and 2%–10% filling factor, metallized with 50 Å of chromium and 200 Å of gold. It is designed to efficiently couple to millimeter-wave radiation and have low heat capacity and low cosmic-ray cross section. Stiff mechanical support consists of strands of silicon nitride 1000 μm long with 3–5 μm^2 cross sectional area connecting the absorber to a silicon frame, with a thermal conductivity of less than 2×10^{-11} W K^{-1}. The design and construction of the micromesh absorbers as well as their optical and mechanical properties are described in Mauskopf et al. (1997).

The thermistor is a rectangular prism of NTD germanium (Haller et al. 1994) 50 μm $\times$ 100 μm $\times$ 300 μm, a factor of 10 times smaller volume than NTD thermistors typically used in composite bolometers. Using these small thermistors decreases the heat capacity of the bolometer by a factor of 5 and increases the fundamental microphonic frequency by a factor of 10. To allow the thermistor to be indium bump-bonded to the micromesh, one of the long faces of the NTD material is metallized with two pads 50 μm wide at either end. Each pad is first implanted with boron and then sputtered with 200 Å of palladium and 4000 Å of gold. Electrical leads, gold pads, and indium bumps are patterned on the micromesh while the silicon nitride still has a solid backing of silicon. Gold pads and indium bumps are deposited at the center of the micromesh on a 300 μm $\times$ 300 μm solid square of silicon nitride. For electrical leads, 200 Å of gold is deposited on some of the support legs of the silicon nitride connecting the pads for the thermistor with large gold pads on the silicon frame. The thermistor is pressed onto the indium bumps, and finally the silicon is etched from the back of the micromesh. The front of the silicon nitride is coated in wax to protect the chip and the metallization during etching. This technique minimizes the amount of material used for reading out the thermistors and therefore minimizes the heat capacity of the device. The indium bump-bonds have survived repeated thermal cycling. A drawing of a micromesh bolometer is shown in Figure 6. The performance of bolometers with indium bump-bonded thermistors is described in Bock et al. (1996).

2.3. *Readout Electronics*

Most bolometric detectors in use today employ a high-impedance semiconductor thermistor biased with a constant current. J-FET preamplifiers have been used to provide a combination of low voltage and current noise well matched to typical bolometer impedances (Halpern 1986) but exhibit excess voltage noise at frequencies typically below a few hertz and have limited the achievable bandwidth of these DC-biased bolometers. At lower frequencies, drifts in the bias current, drifts in the temperature of the heat sink, and amplifier gain fluctuations have been expected to limit the ultimate stability of single-bolometer systems.

AC bridge circuits have been successfully used in many experiments to read out pairs of bolometers with stability to 30 mHz (Wilbanks et al. 1990; Devlin et al. 1994). In this scheme a pair of detectors is biased with an alternating current so that resistance fluctuations are transformed into changes in the AC bias amplitude across each detector. These signals are differenced in a bridge, amplified, and demodulated. The AC signal modulation eliminates the effects of $1/f$ noise in the preamplifiers since the resulting signal spectrum is centered about the carrier frequency. The effects of drifts in the bias amplitude, amplifier gain, and heat sink temperature are greatly reduced if the two detectors in the bridge are well matched. The optical responsivity of each of the detectors in the bridge is equivalent to that of a detector biased with the same rms DC power and is constant in time as long as the average power on the detector is constant over the course of one detector thermal time constant.

BOOMERANG employs an AC-stabilized *total power* readout system for individual bolometers, mounted on a

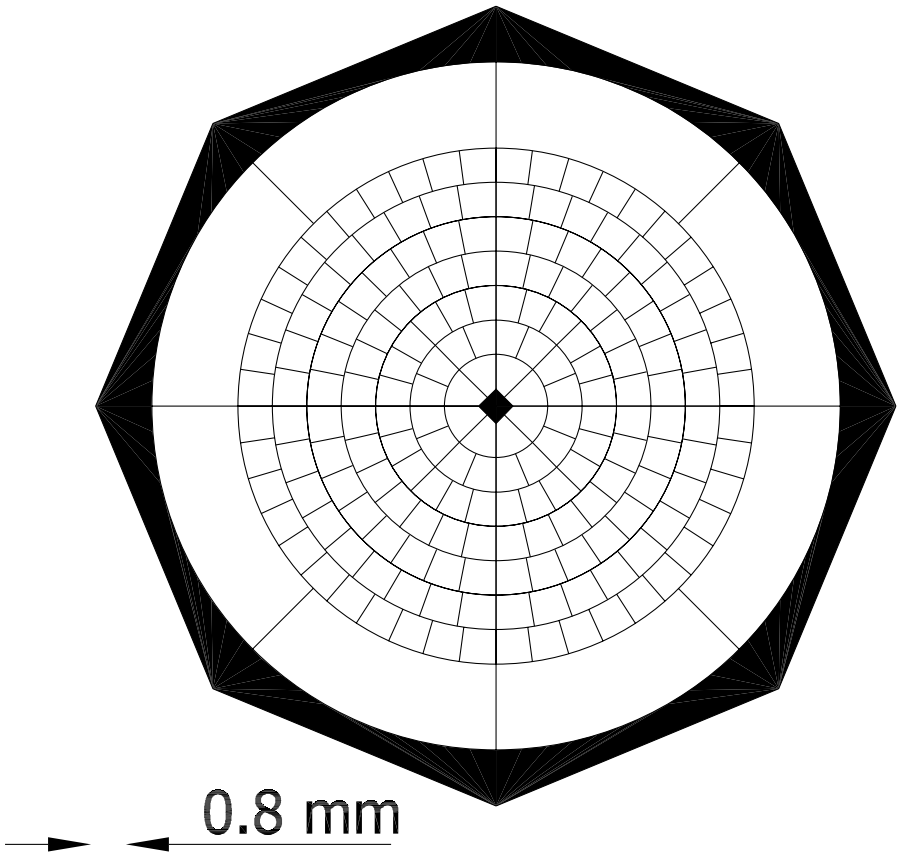

FIG. 6.—Schematic drawing of a micromesh spider web bolometer absorber

temperature-regulated stage (V. Hristov et al. 2002, in preparation). The circuit is summarized in Figure 7.

This system contains a cold J-FETs input stage (based on Infrared Laboratories transimpedance amplifier) and contributes less than 10 nVrms $Hz^{-1/2}$ noise at all frequencies within the bolometer signal bandwidth down to 20 mHz. The warm readout circuit has a gain stability of less than 10 ppm $°C^{-1}$. We remove the large offset due to the background power on the detector with a final-stage high-pass filter with a cutoff frequency of 16 mHz. With this circuit, we have measured the noise spectrum of a low-background micromesh bolometer with $NEP = 1.2 \times 10^{-17}$ W $Hz^{-1/2}$, biased for maximum responsivity to be flat down to a frequency of 20 mHz.

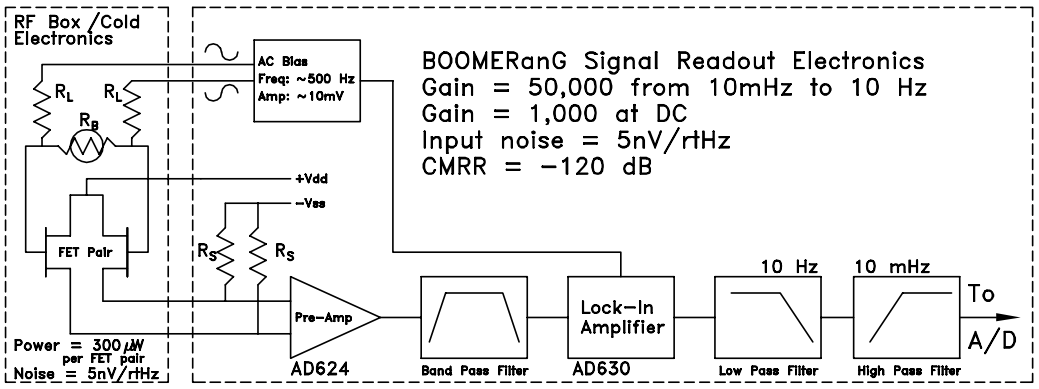

FIG. 7.—Block diagram of the bolometers' readout electronics (one channel shown). The bolometer is AC biased with a differential, low-pass–filtered square wave at ~500 Hz. The AC voltage across the bolometer is modulated by the resistance variations induced by changes in the microwave power absorbed. A matched pair of low-noise J-FETs inside the cryostat reduce the signal impedance from ~10 MΩ down to ~1 kΩ; the signal is then amplified by a differential preamp (AD624), bandpass filtered to remove noise outside the signal bandwidth, and synchronously demodulated by a phase-sensitive detector (AD630). The output of the AD630 is proportional to the instantaneous resistance of the bolometer. Signal components below 10 mHz are attenuated to get rid of $1/f$ noise and drifts using a single-pole high-pass filter. High frequencies (above 10 Hz, i.e., above the cutoff frequency of the bolometer) are also removed by means of a fourth-order low-pass filter. The resulting signal is analog-to-digital converted with 16 bit resolution, at a sampling frequency of 62.5 Hz.

2.4. *RF Filtering*

There are many sources of RFI on the balloon that could couple to bolometers. Microwave transmitters (400 MHz to 1.5 GHz, few watts) that send the data stream to the ground and high current wires that drive the motors of the attitude control system (20 kHz pulse width modulation, several Amps) are situated within a few meters of the cryostat. The BOOMERANG wiring and focal plane are designed to prevent RFI from contributing to the noise of the bolometers.

The bolometers are contained inside a 2 K Faraday cage inside the cryostat. RFI can enter the cryostat through the optical entrance window and propagate into the 2 K optics box. However, the exit aperture of the optics box is RF sealed by the horn-positioning plate. This plate contains feed horns with small waveguide apertures for radiation from the sky to pass through to the detectors. The largest waveguide feedthrough in this plate is 5.1 mm in diameter, which corresponds to a waveguide cutoff of $\sim$35 GHz. Lower frequency RFI is reflected by this surface. Readout wires entering the bolometer Faraday cage can also propagate RF signals as coaxial cables. We run all of the bolometer wires through cast Eccosorb filters mounted to the wall of the Faraday cage to attenuate these signals. The filters are 30 cm long and have a measured attenuation of less than -20 dB at frequencies from 20 MHz to a few GHz.

The readout electronics are also sensitive to RFI. We enclose all of the cryostat electronics in an RF-tight box that forms an extension of the outer shell of the cryostat. The signals from the detectors pass through flexible corrugated stainless steel hoses that are RF sealed to the hermetic connector flange on the cryostat and to the wall of the electronics box. The amplified signals exit the electronics box through Spectrum RF filters mounted on the wall of the box.

2.5. *Cryogenics*

A " heavy duty " ^{3}He fridge and a large ^{4}He cryostat have been developed specifically for the BOOMERANG experiment. A cutaway view of the cryostat is shown in Figure 8.

The main ^{4}He cryostat has to be large enough to contain refocusing optics and a wide focal plane with several multiband photometers. The design and performance of the cryostat and refrigerator are described in detail elsewhere (Masi et al. 1998, 1999). The total volume occupied by the cryogenic section of the receiver is 69 l. The design hold time is about 20 days; the helium tank volume is 60 l; the nitrogen tank volume is 65 l. Conduction thermal input is reduced by suspending both the tanks with Kevlar ropes (1.6 mm diameter). The vibration frequencies of these structures are all above 20 Hz, and the amplitude of the vibrations excited during the flight is expected to be very small. Radiation thermal input on the nitrogen tank is reduced by means of 30 layers of aluminized Mylar for superinsulation. The total thermal input on the nitrogen bath is 6.6 ± 0.4 W.

The radiative thermal load on the L^{4}He is minimized by the use of a vapor-cooled shield. As the liquid helium evaporates, the cold gas flows through a spiral tube that is soldered to the outside of a copper shield that surrounds the helium tank and through a copper heat exchanger that is attached to the top of the vapor-cooled shield before emerg-

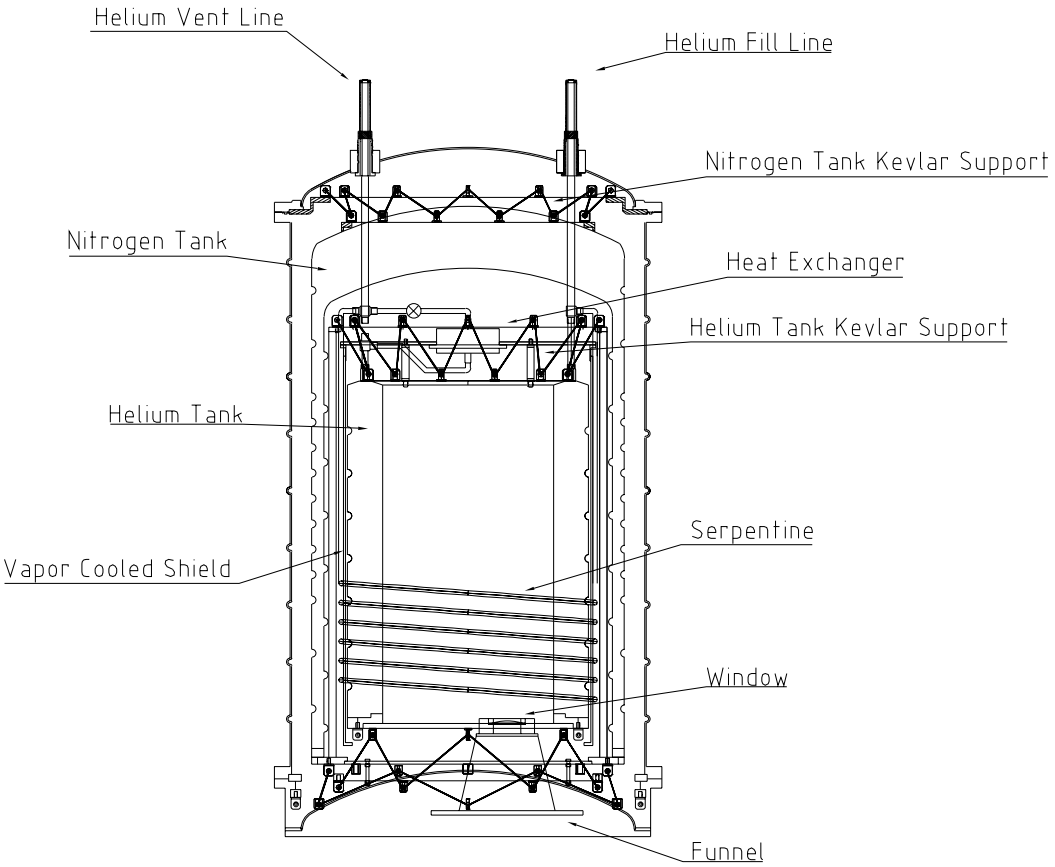

FIG. 8.—Main cryostat. The evaporating ^{4}He gas flows through the serpentine and the heat exchanger to cool a copper shield that minimizes the heat input on the main helium bath. The tanks are supported by Kevlar cord. Nitrogen lines are not shown.

ing from the cryostat. The temperature of the vapor-cooled shield depends on the gas flow rate from the helium tank. During normal operation, the shield remains at a temperature of 15–17 K. The total thermal input on the helium bath is linked to the radiative input through the cryostat window and in flight conditions is about 75 mW.

The cryostat has two circular windows 66 mm in diameter, made with 50 μm polypropylene supported by an aluminum frame.

In the BNA flight we used indium seals able to work at the very low temperature experienced during the night flight ($-50°$C). In the day-time LDB flight it was possible to use rubber (Buna-N) seals since the temperature of the Dewar was always greater than $-30°$C.

The bolometers are cooled by a self-contained ^{3}He fridge shown in Figure 9. The fridge operates with a charcoal sorption pump and can be recycled electronically. During a cycle, hot ^{3}He gas is expelled from the pump by heating it to $\simeq$40 K with a resistance heater. This gas passes through a thin-walled stainless steel tube and condenses on a high-purity copper condensation surface at $\simeq$2 K. The ^{3}He liquid then drops through another stainless steel tube into a 125 cm^3 evaporator pot. Finally, when all of the gas has collected in the evaporator, the heater power is removed from the pump and it is connected to the condensation point with a mechanical heat switch. The pump temperature drops to $\sim$3 K and pumps on the liquid ^{3}He in the evaporator, reducing its temperature to less than 300 mK.

The pump is made of two stainless steel hemispheres crossed by a copper rod that extends outside, to provide thermal attachment points to both the heater and the thermal switch. The pump is connected to the copper condensation plate ($\sim$2 K) through a 1 cm diameter stainless steel tube. There is a 1 cm diameter hole that horizontally passes through the condensation plate, with a 1 cm path to provide more surface area to transfer heat from the ^{3}He gas to the copper. The evaporator consists of a stainless steel cylinder with a 6 cm diameter copper end cap with a ring of 6 mm diameter bolt holes for thermal attachment. The charge is 34 l standard temperature and pressure at 40 bars. The heat load on the ^{3}He stage is about 20 μW. About one-half of this is due to thermal conduction from the condensation point

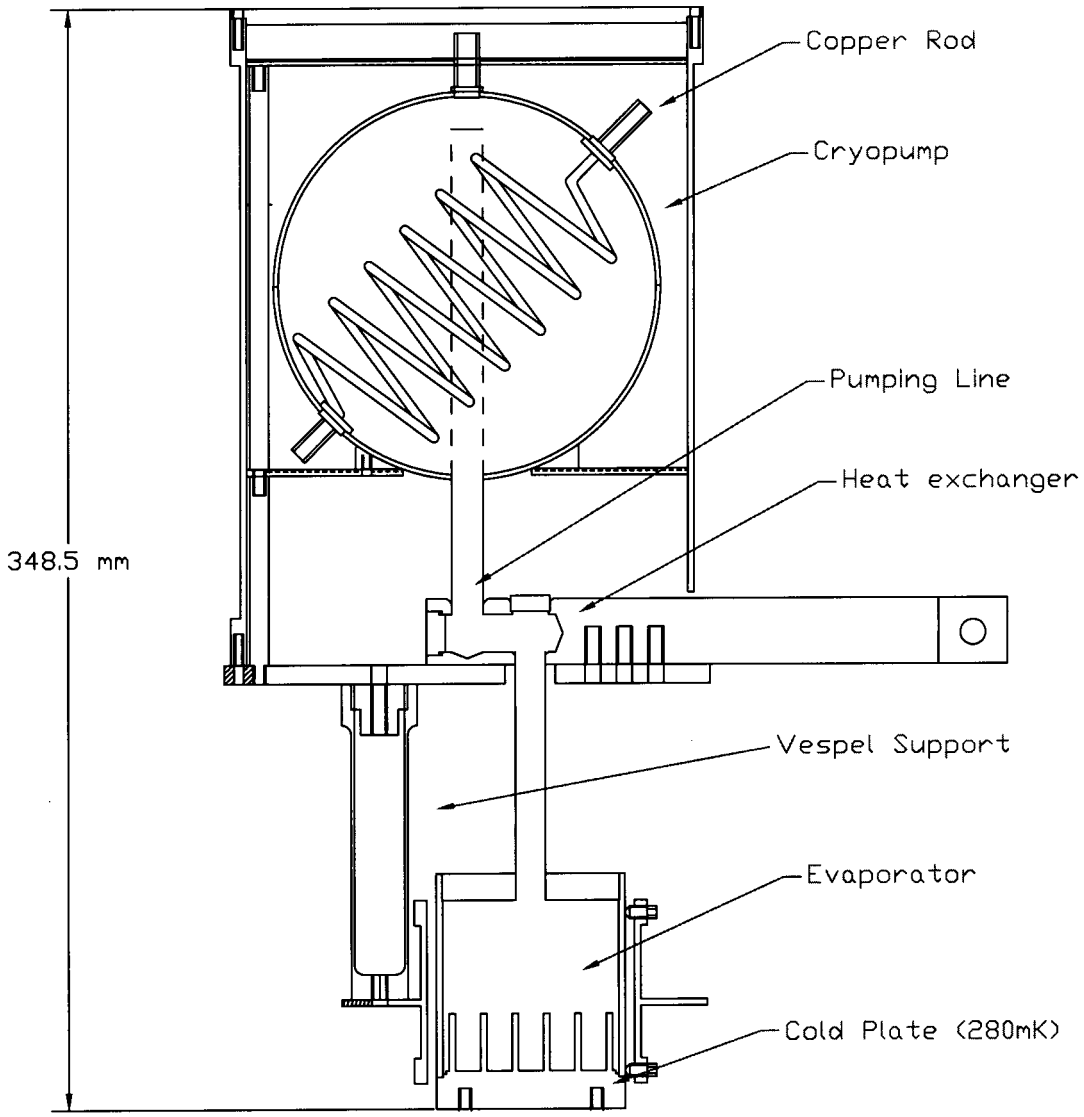

FIG. 9.—BOOMERANG ^{3}He fridge. See description in the text. A mechanical thermal switch, not shown in the drawing, connects the cryopump to the heat exchanger flange.

to the evaporator through the stainless steel pumping tube (9.5 mm internal diameter, 72 mm long, 250 μm thick). The remaining 10 μW is from the mechanical supports for the focal plane. The focal plane weighs 2.5 Kg and must be rigidly held with a mounting structure strong enough to withstand 10 G acceleration in any direction while providing minimal additional thermal input to the ^{3}He fridge. We use four thin-walled Vespel tubes to satisfy these requirements. Vespel has an extremely high strength–to–thermal conductivity ratio at temperatures from 0.3 to 2 K. The tubes are 25.4 mm in diameter, 0.75 mm thick, and 75 mm long. The yield strength of a tube can be calculated from standard formulae. The criterion we use for strength is that the maximum deflection be less than 1% of the elastic limit of the material. Additional heat load from electrical leads is minimized by the use of 125 μm diameter manganin wires that run up the length of the Vespel tubes between the cold J-FET amplifier box and the detectors. The wires are firmly attached to fixed surfaces along their entire length with Teflon tape to eliminate vibrations, which can make the detectors microphonically sensitive. The length of the wires is minimized to reduce their contribution to the input capacitance at the J-FETs. The RC cutoff frequency for a 5 MΩ detector impedance is measured to be greater than 2 kHz, for an input capacitance of less than 40 pF.

During observations, the temperature of the focal plane can be maintained constant with a high-precision temperature regulation circuit (V. Hristov et al. 2002, in preparation). In fact, temperature fluctuations of the 300 mK stage can contribute to excess bolometer noise. The temperature of the bolometer is determined by

$$T_{\rm bolo} = T_0 + \frac{P_{\rm opt}}{\int_{T_0}^{T_{\rm bolo}} \kappa_0 T^\alpha dT} , \quad (4)$$

where $P_{\rm opt}$ is the optical power on the detector and $\int_{T_0}^{T_{\rm bolo}} \kappa_0 T^\alpha dT$, indicated as $G_{\rm eff}$ (W K^{-1}) hereafter, is the effective thermal conductivity per unit of temperature between the thermistor and the bath at T_0. Therefore, the change in bolometer temperature for a change in base plate temperature is given by

$$\Delta T_{\rm bolo} = \beta \Delta T_0, \quad (5)$$

where β is a constant of order unity. The bolometer NEP is related to these temperature fluctuations by

$$\mathrm{NEP}_T = G_{\rm eff} \Delta T_{\rm bolo} , \quad (6)$$

where NEP_T is in W Hz$^{-1/2}$ and $\Delta T_{\rm bolo}$ (K Hz$^{-1/2}$) is the spectrum of temperature fluctuations. Therefore, the condition for temperature stability of the cold stage is $\mathrm{NEP}_T < \mathrm{NEP}_{\rm bolo}$. For the BOOMERANG bolometers with $G_{\rm eff} = 8 \times 10^{-11}$ W K^{-1} and $\mathrm{NEP}_{\rm bolo} \simeq 2 \times 10^{-17}$ W Hz$^{-1/2}$, the requirement for the stability of the cold stage is

$$\Delta T_{\rm bolo} < 250 \text{ nK Hz}^{-1/2} . \quad (7)$$

Two NTD thermistors are mounted on the 300 mK stage and read out with DC-coupled bridge circuits. One channel is used as the control sensor, and the other is a monitor sensor. We measure the spectrum of fluctuations from the monitor channel while the temperature regulation circuit is running to be flat down to less than 30 mHz with an amplitude of 40 μVrms Hz$^{-1/2}$, corresponding to a temperature stability of 120 nK Hz$^{-1/2}$. This is better than is needed to ensure that the BOOMERANG bolometers do not have a significant noise contribution from temperature fluctuations.

2.6. *Pressure Control Systems*

The pressure on the main helium bath is maintained around 10 mbar in lab and in flight to keep the bath temperature below 2 K, while the pressure on the nitrogen bath is kept around 1 atm to prevent the formation of fluffy solid. We used two pressurization systems. The helium pressurization system allows us to pump on the bath at ground and to open to atmosphere pressure at float by means of a motorized high vacuum seal valve. The nitrogen system controls the pressure using an absolute sensor and three electrovalves. Both systems have relief valves to allow safety and functionality even in the case of electronic failures.

2.7. *Internal Calibrator*

An internal calibrator in the reimaging optics box allows us to monitor the detector sensitivity during flight. The calibrator consists of a high-background bolometer with an NTD-4 Ge thermistor (Haller et al. 1994) attached to the center of a 5.6 mm diameter silicon nitride absorber, electrically connected with 0.001 inch diameter copper leads. The calibrator is mounted on the 2 K stage directly behind a 1 cm hole in the center of the tertiary mirror, where all of the beams from the concentrating horns are coincident. The calibrator can be heated with a current pulse to give a temperature rise of several kelvins with a recovery time of a few milliseconds. The corresponding power on the detectors is

$$P_{\rm cal} \simeq 2k\Delta T_{\rm cal} \frac{\nu^2}{c^2} \Delta\nu \Omega \epsilon f , \quad (8)$$

where ϵ is the calibrator efficiency and f is the effective Lyot stop fraction area filled by the calibrator. This corresponds to an equivalent signal on the sky of

$$\Delta T_{\rm CMB} = \epsilon \Delta T_{\rm cal} f . \quad (9)$$

Response to the internal calibrator during flight for one of the detectors is shown in Figure 10. The equivalent signal on the sky is $\sim$175 mK.

3. ATTITUDE CONTROL SYSTEM

The attitude control system (ACS) must be able to point in a selected sky direction and track it or scan over it with a reasonable speed. The specifications are 1′ rms for pointing stability, with a reconstruction capability better than $\sim$0.′5 maximum. Our main modulation is obtained scanning in azimuth, with a sawtooth scan, with an amplitude of 40° (peak to peak) and a scan rate of about 2° s^{-1}. We have developed an ACS for BOOMERANG with these capabilities based on the ACS systems designed and built for the ARGO and MAX-5 experiments (de Bernardis et al. 1993; Tanaka et al. 1996). The BOOMERANG ACS is based on a pivot that decouples the payload from the flight chain and controls the azimuth, plus one linear actuator controlling the elevation of the inner frame of the payload. The pivot has two flywheels, moved by powerful torque motors with tachometers. On the inner frame, which is steerable in eleva-

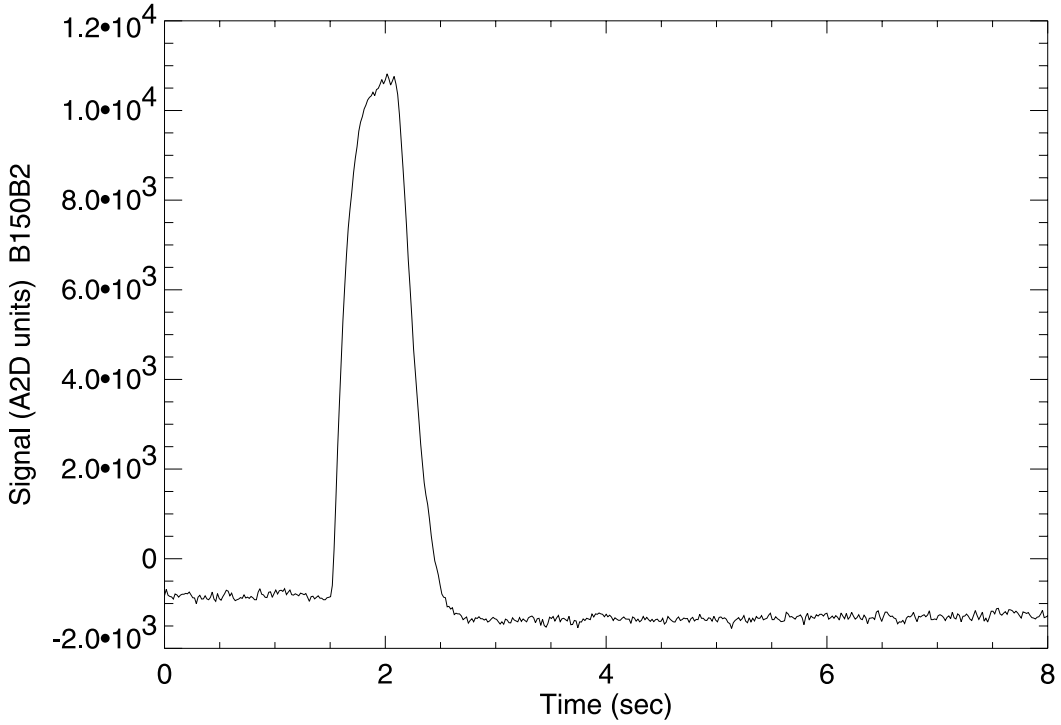

FIG. 10.—Bolometer signal during a pulse from the internal calibrator. A/D units are used, corresponding to a full scale of ±10 V in 16 bits.

tion with respect to the gondola frame, are mounted both the telescope and the cryogenic receiver. The observable elevation range is between 33° and 65°. The sensors are different for night (North America) and day (Antarctic) flights. For night flights we have a magnetometer and an elevation encoder; additional information on the average attitude is obtained by means of a sensitive tilt sensor. A CCD star camera is used outside the feedback loop for absolute attitude reconstruction. A CPU handles commands and observation sequencing; the same CPU digitizes sensor data and controls the current of the three torque motors.

3.1. *CCD Star Camera*

We used a video CCD camera (Cohu 4910) with a large-aperture lens (Fujinon CF50L) as a star sensor. The focal length is 50 mm; the numerical aperture is f/0.7. The CCD format is $\frac{1}{2}''$, and the video signal is RS-170 at 60 Hz. The image area in the CCD is 6.4 mm × 4.8 mm, with 768 × 494 pixels. The resulting field angle is 7°.30 × 5°.50. The optics are baffled to protect the lens input against stray rays from reflecting surfaces in the payload. The baffle is a corrugated cylindrical structure painted black on the internal surface and dimensioned for complete protection of the lens input. We removed the CCD protection glass in order to accommodate the lens output surface close enough to the CCD chip surface. Boresight between the star camera and the millimeter-wave telescope is trimmed at ground and cannot be changed in flight. The CCD is mounted on the gondola through fiberglass supports and is surrounded by a protective and thermally insulating foam box. A few resistors, dissipating a total of ~10 W, are used to keep the system warm.

CCD images are processed on board in real time. We used a Matrox Image-LC board as a frame grabber and signal processing unit (DSP). The board accepts an analog (video) input and returns a VGA output image. The star sensor computer is connected to the other flight computers through serial ports. These electronics were assembled inside a pressure vessel in order to let the system operate at standard pressure during the flight. This is required for both the correct operation of the hard disk and the thermalization of the components. A thermostat and two fans inside the vessel control the internal air temperature. The total heat dissipation of the system is ~50 W. When the fans are operating, the heat-dissipating devices are thermally connected to the outer shell of the vessel, radiating away the heat and effectively cooling the system. If the air gets too cold, the fans stop, effectively insulating the system. In this way we can maintain the operation temperature close to 20°C during the flight, despite the low temperature (~230 K) and pressure (~3 mbar). We used the Matrox Imaging Library package for the in-flight star recognition software in an optimized C code. The image analysis algorithm uses *blob analysis* to select the two brightest stars in the field. The system is able to compute and transmit the pixel and brightness information 5 times s^{-1}.

Before the flight we tested the performances of the CCD and of the optics in a vacuum chamber at room temperature and at $T \simeq 240$ K. We found a small increase of the sensitivity of the CCD at lower temperature, while there is no detectable defocusing of the image.

The sensitivity of the camera was checked observing a star field from the Campo Imperatore Astronomical Observatory (at an altitude 2200 m above sea level). It was possible to identify sources of magnitude $m \leq 6.5$, not far from the sensitivity we obtained during the flight.

When tested with suitable sources (i.e., stars with $m \leq 4$ and negligible seeing, as at float), the camera produces tar-

gets by positions of the centroid determination accurate to 1/10 of a pixel ($\sim 3''$).

The alignment of the CCD axis with the microwave beam was obtained by observing a strong chopped thermal source placed at a distance of $\sim$120 m and correcting for the parallax due to the offset between the millimeter-wave telescope and the camera (540 mm in the meridian axis, 640 mm in the horizontal axis). We also tested the tilt of the CCD field with respect to the horizontal axis performing pure azimuthal scans on the same source. We reduced the tilt below 2–3 pixels along a 6° azimuthal scan.

Since not all frames have two stars present, the pointing was recontructed between good frames by integrating the data from the gyroscopes (sampled at 10 Hz). This led to a precision of less than $1'$ rms in the pointing solution.

Pendulations of the gondola were monitored by roll and pitch gyroscopes. The typical power spectrum of the pitch fluctuations is reported in Figure 11.

4. SCAN STRATEGY

The BOOMERANG scan strategies are designed to obtain high signal-to-noise ratio (S/N) measurements of CMB anisotropies covering as wide a range of angular scales as possible, limited only by the functional bandwidth of the detectors. The maximum scan speed is limited by the mechanics of the ACS and by the thermal time constant of the bolometers. The minimum scan speed is set by the stability of the detectors, readout electronics, and sources of local emission. The ratio of these maximum and minimum signal frequencies for the BOOMERANG detectors is $\approx$30, allowing us to cover a range in angular scale, corresponding to multipoles $10 < \ell < 900$.

The range of spatial frequencies, or multipole number ℓ, that we sample depends primarily on the beam size. Because we use bolometric detectors, we are free to select any beam size at a given wavelength equal to or larger than the diffraction limit, $\theta_{\rm diff} = 1.22\lambda/D$, where D is the diameter of the illumination pattern on the primary that is fixed for all channels by the Lyot stop to be 85 cm. The throughput for such a system is a function of the beam size:

$$A\Omega(\lambda, \theta) = \lambda^2 \left(\frac{\theta}{\theta_{\rm diff}} \right)^2 . \quad (10)$$

The optical loading on the detector and the optimal thermal conductance, G, are proportional to the throughput, $A\Omega$. The absorbing area of the detectors also must be proportional to $A\Omega$; however, the heat capacity, C, of the micromesh bolometers is dominated by the thermistor, so it is independent of throughput. Therefore, the time constant of optimized bolometers decreases as the beam size increases, $\tau \propto 1/(A\Omega)$. In addition, the signal from the CMB is proportional to the throughput, but the detector noise increases as the square root, so that the sensitivity to CMB fluctuations improves as $\sqrt{A\Omega}$. Therefore, overmoded bolometers are faster and more sensitive than diffraction-limited channels. We can make use of this to scan faster and cover a larger area of sky with overmoded channels with high sensitivity and scan slower and obtain higher angular resolution with diffraction-limited channels. We have optimized each BOOMERANG focal plane for angular resolution and sensitivity.

The BOOMERANG North American flight, in 1997 August, covered a region of sky approximately 700 deg^2 (Fig. 12). This region was selected to have a low column density of dust as estimated from the IRAS 100 μm meas-

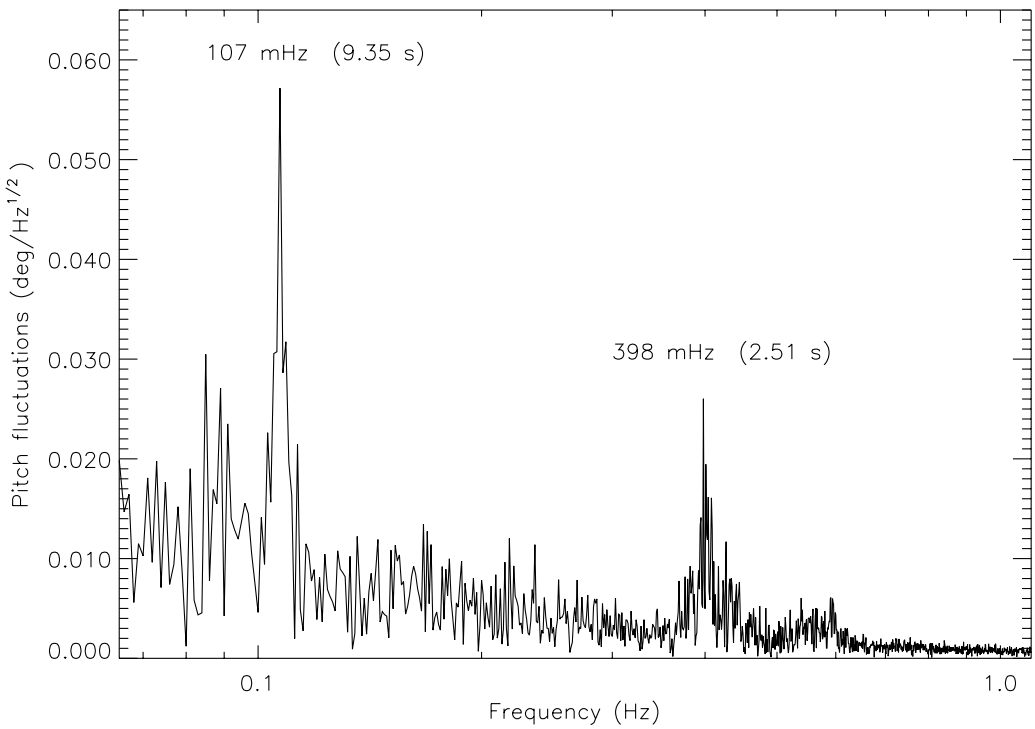

FIG. 11.—Power spectrum of the pitch of the payload during scans. Small pendulations are at 107 and 398 mHz, corresponding to periods of 9.35 s (full flight chain) and 2.51 s (payload).

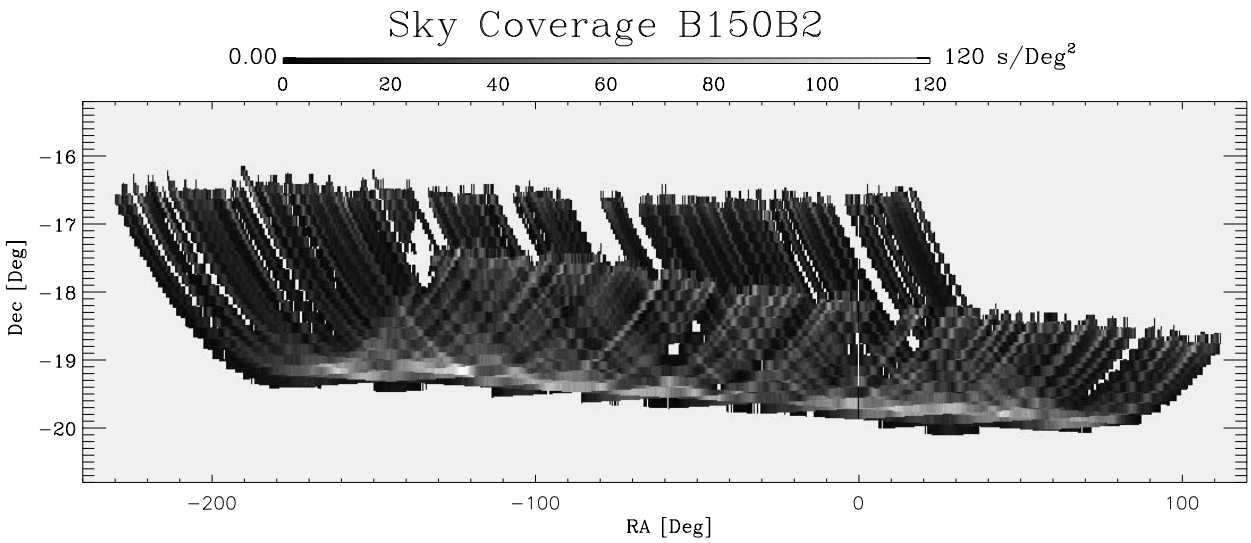

FIG. 12.—Sky coverage and integration time distribution during the flight of 1997 August 30

urements and provided even sky coverage with an appropriate integration time per pixel based on our detector sensitivity estimates. The focal plane shown in Figure 3 contained 2 40′ pixels at 90 GHz and 4 20′ pixels at 150 GHz. The gondola was scanned continuously in a triangle wave with peak-to-peak amplitude of 40° and a maximum scan velocity of 2° s^{-1}, corresponding to ~2 bolometer time constants per beam.

5. PREFLIGHT CALIBRATION

The preflight calibration procedure is performed before declaring flight readiness, in order to have a precise forecast of the flight performance of the instrument. For our telescope and receiver the most important tests are as follows.

1. Bolometers load curves under different radiative loads. This is performed filling the photometer beam with blackbody loads at room temperature and at 77 K and inserting in the beam a cold attenuator, with 1% transmission, to simulate the in-flight radiative background. Results for throughput and optical efficiency are in Table 4.

2. Voltage noise measurements of the system were performed to estimate the sensitivity and to check for 1/f noise in the detectors. Results are in Table 5. In addition, a preliminary measure of the detectors' time constants τ was done to have an indication of performance. This measurement has to be repeated in flight in order to have the correct values, which are strongly dependent on the background radiation (see § 6.1).

3. Spectral characterization was made using a lamellar grating interferometer with an Hg vapor lamp as Rayleigh-Jeans source. A check for near-band leak in the optical filters was made by means of three thick grill filters at 4.9, 7.7, and 10.5 cm^{-1}, which reduced the integrated signal by more than a factor of 100 in the corresponding bands.

4. Beam profiles ware measured using a collimated source, filling the telescope acceptance area. The wide (1 m diameter) parallel beam is produced by a thermal source in the focus of a large parabolic reflector.

TABLE 4
PREFLIGHT THROUGHPUT AND OPTICAL EFFICIENCY CALIBRATION FOR THE SIX DETECTORS

Channel	Throughput (cm^2 sr)	Optical Efficiency
NA-B150A1...	0.11	8%
NA-B150A2...	0.08	19%
NA-B150B1...	0.11	8%
NA-B150B2...	0.08	20%
NA-B90A	0.27	7%
NA-B90B.....	0.27	9%

TABLE 5
PREFLIGHT VOLTAGE NOISE MEASUREMENTS

Channel	Noise (nV $Hz^{-1/2}$)	1/f Knee (Hz)	Responsivity (W)	NEP (W $Hz^{-1/2}$)	NET_{CMB} ($\mu K\ s^{-1/2}$)
NA-B150A1...	12	0.8	4.5×10^8	2.6×10^{-17}	260
NA-B150A2...	12	0.2	3.1×10^8	3.8×10^{-17}	220
NA-B150B1...	16	0.5	4.4×10^8	3.6×10^{-17}	360
NA-B150B2...	11	<0.1	3.6×10^8	3.1×10^{-17}	160
NA-B90A	12	0.8	4.7×10^8	2.6×10^{-17}	210
NA-B90B.....	14	0.8	3.5×10^8	4.0×10^{-17}	240

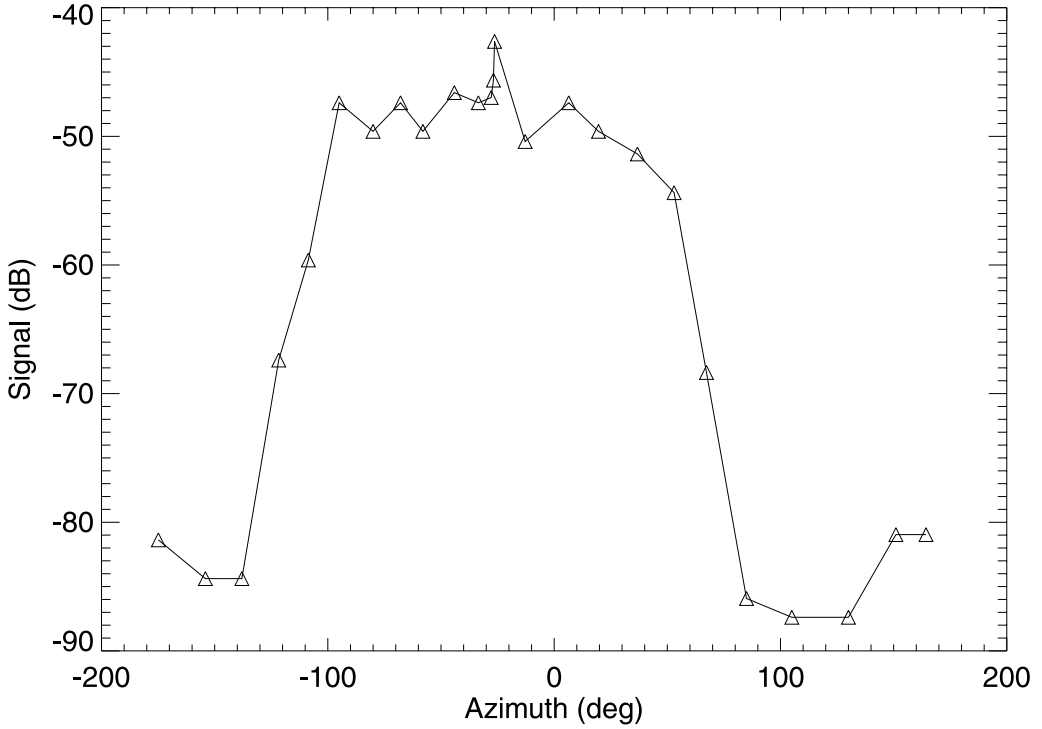

FIG. 13.—Sidelobe measurements at ground. The source is positioned at an elevation of 39°, while the telescope is pointed at 49° during this scan. The sharp cutoff at large angles is due to the effect of the large Sun shields.

5. Sidelobe measurements or upper limits. We have illuminated the fully integrated payload using a high-power (30 mW) 90 GHz Gunn oscillator, completed with calibrated attenuators and high-gain horn (20° FWHM). The microwave source was electronically chopped at 11 Hz. The payload was located at the center of a wide, flat area, and the source was set up at a distance of ~50 m from the payload, at an apparent elevation of ~39°, so that the microwave beam overilluminated the payload. We first boresighted the BOOMERANG telescope to the fully attenuated microwave source, to record the axial gain of the instrument. We then rotated the payload in azimuth, reducing the source attenuation as necessary, to record the far sidelobe response of the instrument for different off-axis locations of the source. We made several spins, with different apparent elevations of the source. Results for a sample elevation are reported in Figure 13.

6. OBSERVATIONS AND IN-FLIGHT PERFORMANCE

The system was flown for 6 hr on 1997 August 30 from the National Scientific Balloon Facility in Palestine, Texas. All the subsystems performed well during the flight: the He vent valve was opened at float and was closed at termination; the nitrogen bath was pressurized to 1000 mbar; the ^{3}He fridge temperature (290 mK) drifted with the ^{4}He temperature by less than 10 mK during the 7.5 hr of the flight, with a maximum temperature of 300 mK before venting to atmosphere and slowly drifting down to 290 mK. The main ^{4}He cryostat wormed to 2.05 K during ascent and then recovered to 1.65 K. Pendulations were not generated during CMB scans at a level greater than 0.′5, and both azimuth scans at 2° s^{-1} (see Fig. 14) and full azimuth rotations (at 2 and 3 revolutions per minute [rpm]) of the payload were performed effectively. The loading on the bolometers was as expected, and the bolometers were effectively CR immune, with white noise ranging between 500 and 1000 μK Hz$^{-1/2}$.

Measurements of the in-flight performance (time constants, beam mapping, and calibration constants) are essential to a good determination of the power spectrum of the anisotropies. The measured power spectrum is in fact the convolution of the real power spectrum with an angular function given by the shape of the beam (see Fig. 15), and the amplitude of the spectrum depends on the calibration constant.

6.1. *In-Flight Time Constants of the Bolometers*

The total transfer function of the system is the combination of the electronics and the bolometer transfer functions. A high-pass filter ($\tau \sim 10$ s) and a two-pole Butterworth low-pass filter determine the electronic transfer function, which was measured in lab. From equation (3) we see that the bolometer behaves like a low-pass filter with a time constant $\tau = C/G$. The value of τ changes with the temperature of the receiver and with the radiative input and has to be measured in flight. For a given input [IN(t)] on the bolometer, the output [OUT(t)] of the system with transfer function $T(\omega)$ (bolometer and electronics) is

$$\mathrm{OUT}(t) = \mathrm{IFT}(\mathrm{FT}(\mathrm{IN}(t)) \times T(\omega)) \, , \qquad (11)$$

where FT and IFT are the Fourier transform and inverse Fourier transform operator, respectively. It is possible to fit the parameters in the $T(\omega)$ using the OUT(t) data. As input we use the signal from a planet in a fast scan mode. When the scan speed is 3 rpm (18° s^{-1}), the time of transit of the planet in the beam (less than 40′) is

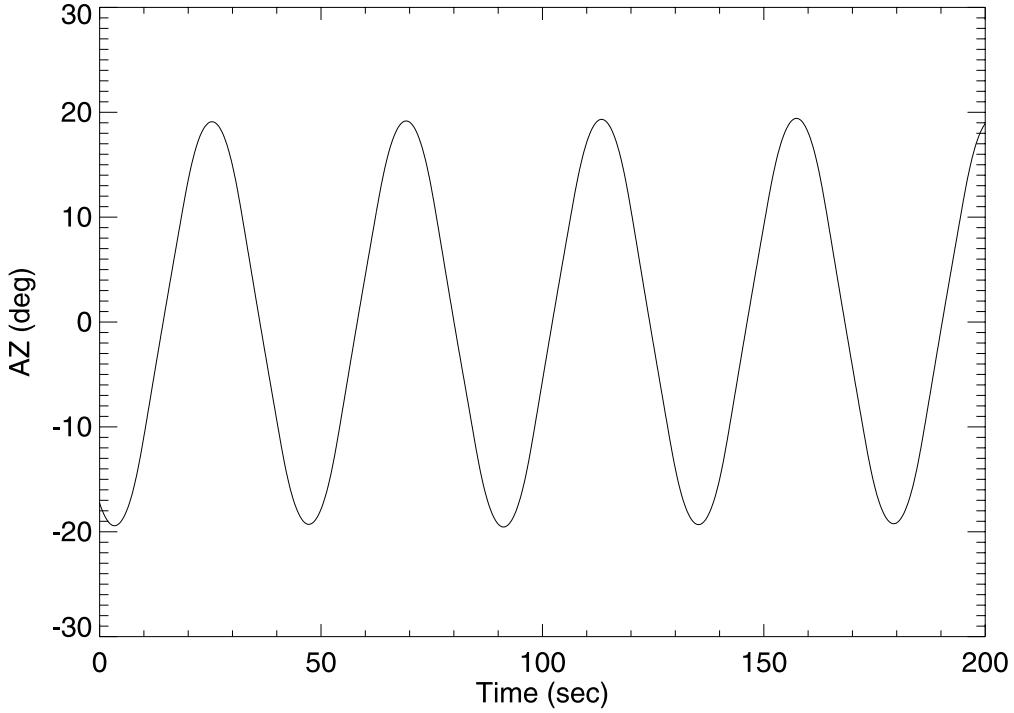

FIG. 14.—Azimuth read by the magnetometer during a scan. The amplitude is $\pm 20°$; the shape is a smoothed sawtooth function. In this configuration the fraction of the scan at constant speed fraction is about one-half of the total.

about the time of two samples (sampling rate is 62.5 Hz). Thus, the IN(t) signal has to be modeled with a beam shape function. Simulations show that for this sample rate and scan speed the results are the same within the error, assuming either Gaussian or square beam. The measured time constants are reported in Table 6. These values are longer than expected for spider web bolometers. The source of the problem was tracked to excess heat capacity of the chromium layer and was corrected for the devices used in the subsequent LDB flight.

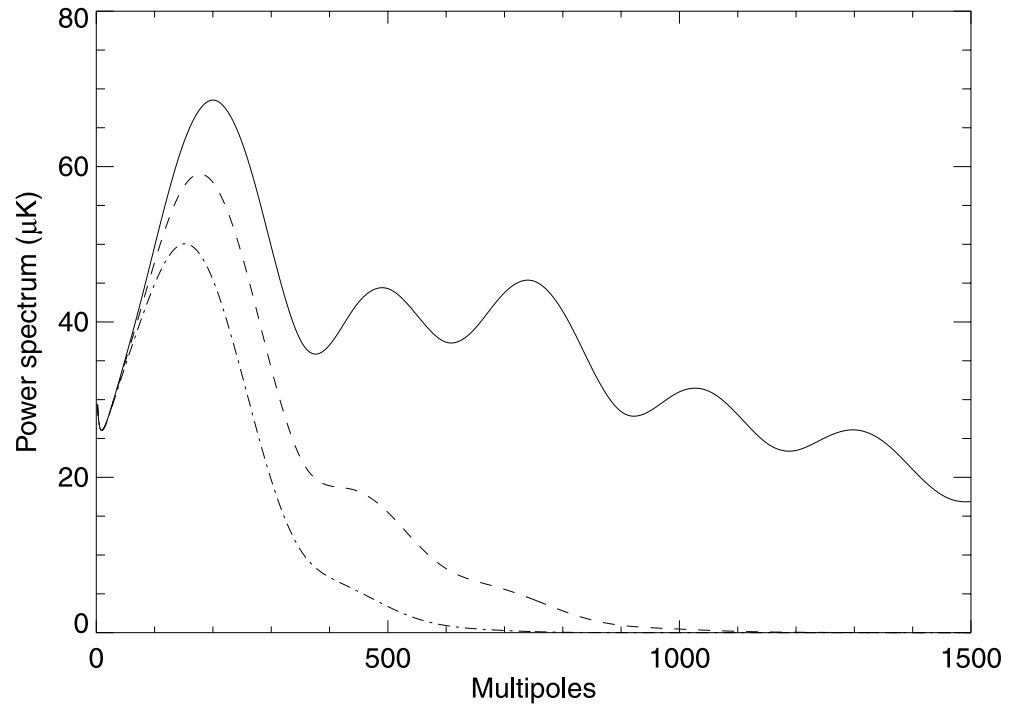

FIG. 15.—Convolution of the best-fit power spectrum of CMB anisotropy (Mauskopf et al. 2000) with the BNA beams. The continuum line is the original power spectrum, the dashed line is the convolution with a 150 GHz channel (16′.6 FWHM), and the dot-dashed line is the convolution with a 90 GHz channel (26′.0 FWHM). The importance of a good determination of the beam shape is evident.

TABLE 6
IN-FLIGHT TIME CONSTANTS OF THE BOOMERANG NA BOLOMETERS

Channel	Time Constant (ms)
NA-B150A1 ...	102 ± 11
NA-B150B1 ...	83 ± 13
NA-B150B2 ...	83 ± 12
NA-B90A	165 ± 9
NA-B90B.....	71 ± 8

NOTE.—All values except NA-B150B2 are calculated from fast scans across Jupiter. The NA-B150B2 value is calculated by comparing that detector's cosmic-ray signals with those of NA-150B1, which are the same to within error.

6.2. *Jupiter Calibration and Beam Mapping*

During the 1997 August North American flight of BOOMERANG, we calibrated the instrument and produced a detailed beam map by scanning the planet Jupiter (de Bernardis, DeTroia, & Miglio 1999). In addition, we made a secondary calibration through measurements of the CMB dipole, which is known to $\simeq 1\%$ accuracy from the measurements of the *COBE* satellite (Kogut et al. 1993).

The responsivity of the instrument is defined as

$$\mathscr{R} = \frac{\Delta V}{\Delta W} , \tag{12}$$

where ΔW is the radiative input and ΔV the output of the bolometers. The calibration constant directly converts the signal in volts into CMB temperature (in kelvins) and is defined as

$$\mathscr{K} = \frac{\Delta V}{\Delta T_{\rm CMB}} . \tag{13}$$

The use of planets for calibration is standard in midlatitude CMB experiments. Planets are bright sources, and their millimeter-wave brightness temperature is known at the 5% level. Moreover, they are pointlike sources when compared to our beam, so they are perfectly suitable for mapping the shape of the beam pattern of the telescope.

The signal from the planet is

$$\Delta V_{\rm planet} = \mathscr{R} A \Omega_{\rm planet} \int E(\nu) {\rm BB}(T_{\rm eff}, \nu) d\nu , \tag{14}$$

where $T_{\rm eff}$ is the brightness temperature of the planet, $E(\nu)$ is the spectral efficiency, and $\Omega_{\rm planet}$ is the (small) solid angle filled by the planet as computed from the ephemerides on the day of the observation. The CMB signal is related to the derivative of the Planck function with respect to the temperature:

$$\Delta V_{\rm CMB} = \mathscr{R} A \Omega \frac{\Delta T_{\rm CMB}}{T_{\rm CMB}} \int E(\nu) {\rm BB}(T_{\rm CMB}, \nu) \frac{x e^x}{e^x - 1} d\nu , \tag{15}$$

where $A\Omega$ is the throughput of the system, $x = h\nu / k T_{\rm CMB}$, and ${\rm BB}(\nu, T)$ is the Planck function. Note that the beam solid angle Ω is the angular response function $RA(\theta, \Phi)$ integrated over all the angles:

$$\Omega = \int_{4\pi} RA(\theta, \Phi) \cos\theta \sin\theta \, d\theta \, d\Phi . \tag{16}$$

From equations (14) and (15) the resulting expression for the calibration constant is

$$\mathscr{K} = \frac{\Delta V_{\rm CMB}}{\Delta T_{\rm CMB}} = \frac{\Delta V_{\rm planet}}{T_{\rm CMB}} \frac{\Omega}{\Omega_{\rm planet}} \frac{\int E(\nu) {\rm BB}(T_{\rm CMB}, \nu) x e^x (e^x - 1)^{-1} d\nu}{\int E(\nu) {\rm BB}(T_{\rm eff}, \nu) d\nu} . \tag{17}$$

$E(\nu)$ has been measured in the laboratory, $\Delta V_{\rm planet}$ is the maximum signal from the planet, and Ω can be determined from a raster scan on the planet.

The telescope made two series of scans on Jupiter with an amplitude of 15° and a speed of $1\overset{\circ}{.}1\ {\rm s}^{-1}$. Jupiter has an effective source temperature of $T_{\rm eff} = (173 \pm 9)$ K (Ulich 1981; Goldin et al. 1997). The data have a high S/N (greater than 100; see Fig. 16) and permit the production of the beam profile of each receiver. The solid angles Ω are computed integrating the angular response, $RA(\theta, \Phi)$, given by the pixelized Jupiter map. Errors are given by the pointing error and the noise. The beams are symmetric, with minor and major axes equivalent within 5%. FWHMs are computed averaging the data in annuli around the center and fitting the shape with a Gaussian function (see Fig. 17).

Solid angles and FWHMs are summarized in Table 7. The calibration constants are in Table 8.

6.3. *Dipole Calibration*

The dipole (Fixsen et al. 1994) is a well-calibrated source, featuring the same spectrum as CMB anisotropies and completely filling the beam of CMB anisotropy experiments. It is available at any time during the observations, thus allowing repeated checks for the calibration of the experiment. If a scanning experiment can perform large-scale scans, the dipole will appear as a scan synchronous signal with an amplitude $\Delta T_{\rm dipole}$ of the order of a few millikelvins (depending on the actual scan geometry), thus perfectly suitable for calibration. The calibration constant is simply

$$\mathscr{K} = \frac{\Delta V_{\rm dipole}}{\Delta T_{\rm dipole}} , \tag{18}$$

where $\Delta V_{\rm dipole}$ is the amplitude of the signal during dipole observations. The precision of this measurement is affected by the presence of atmospheric emission and by $1/f$ noise of the system. The BNA bolometers showed noise spectra white down to 10 mHz. In these conditions it is possible to make dipole scans with a period of the order of 1 minute without being significantly affected by $1/f$ noise.

Dipole scans consisted of full azimuth revolutions of the gondola at $18^\circ\ {\rm s}^{-1}$ and were carried out for 10 minutes every hour. The instantaneous S/N of the dipole scans was ~ 3. Raw data from one of the dipole scans are shown in Figure 18.

In Figure 19 we plot the azimuth of the maximum dipole signal versus the azimuth of the CMB dipole as observed

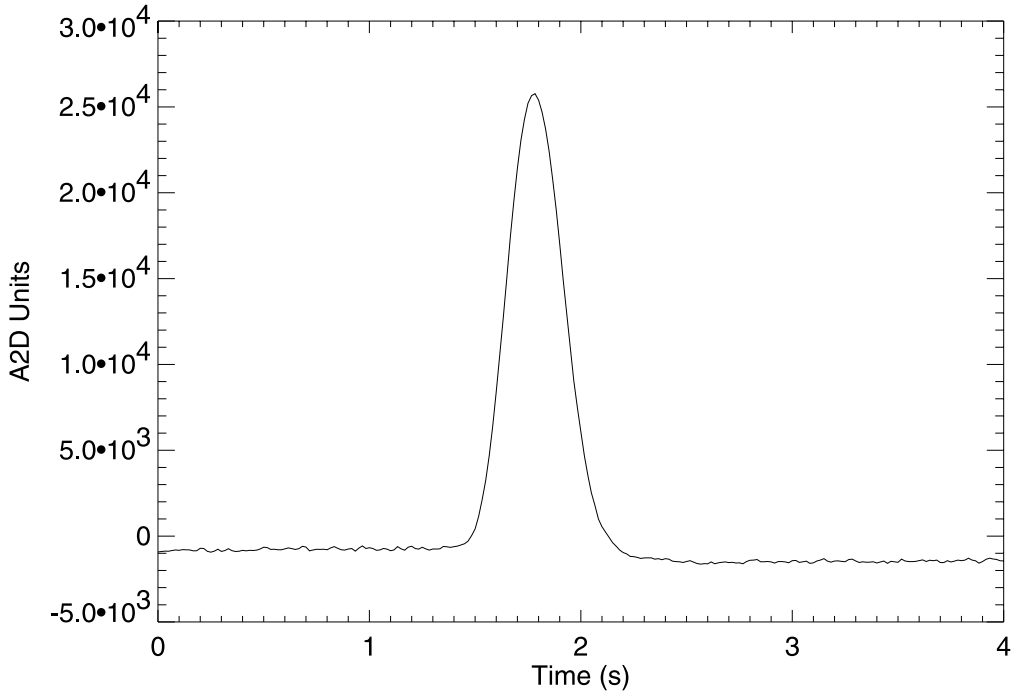

FIG. 16.—Raw data of a single scan on Jupiter at 150 GHz. S/N is greater than 100; scan speed is $1^{\circ}.1\ s^{-1}$. The negative tail of the data is due to the AC coupling of the signal.

from the payload position at the time of the observations, thus providing evidence for detection of the CMB dipole and convincingly rejecting any hypothesized local origin of the signal.

The CMB dipole calibration in the first set of revolutions is consistent with Jupiter calibration performed immediately before (see Table 8). We note however that the dipole signal shape and size changes in the subsequent set of rotations for both B90B and B150B2 channels, producing calibrations not completely consistent with those derived from the internal calibrator (see Fig. 20).

Even if the atmospheric emission is greatly reduced at balloon altitude (greater than 35 km), large-scale fluctuations of the atmospheric brightness might not be negligible with respect to the CMB dipole, thus giving a contamination at large scales hard to remove without a monitoring high-frequency (240, 400 GHz) channel (Page, Cheng, & Myers 1990; Lee et al. 1999). For this reason we have used the Jupi-

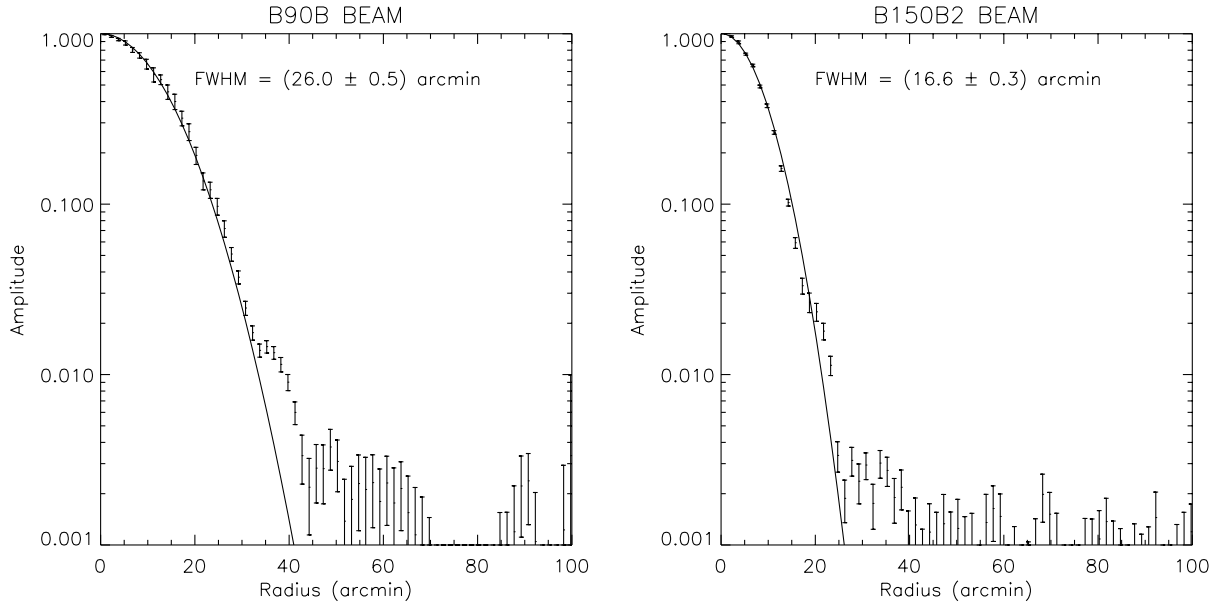

FIG. 17.—Jupiter data averaged in annuli around the centroid and Gaussian fits. The small shoulders evident at the few percent level are real and are due to aberrations in the optical system.

TABLE 7
BEAM SIZE MEASUREMENTS FOR THE BOOMERANG NA TELESCOPE

Channel	FWHM (arcmin)	Ω (sr)
NA-B150A1...	19.5	$(3.04 \pm 0.17) \times 10^{-5}$
NA-B150B1 ...	19	$(3.03 \pm 0.25) \times 10^{-5}$
NA-B150B2 ...	16.6	$(2.63 \pm 0.10) \times 10^{-5}$
NA-B90A	24	$(5.61 \pm 0.36) \times 10^{-5}$
NA-B90B.....	26	$(6.47 \pm 0.27) \times 10^{-5}$

TABLE 8
CALIBRATION CONSTANTS FOR THE BOOMERANG NA TELESCOPE

Channel	$\mathscr{K}_{\rm Jupiter}$ (nV mK^{-1})	$\mathscr{K}_{\rm dipole}$ (nV mK^{-1})
NA-B150A1...	57.1 ± 5.1	54.1 ± 3.2
NA-B150B1 ...	59.9 ± 7.8	53.0 ± 2.1
NA-B150B2 ...	71.4 ± 5.7	66.4 ± 1.5
NA-B90A	48.1 ± 8.2	43.1 ± 1.1
NA-B90B.....	60.9 ± 8.5	61.9 ± 2.5

NOTE.—The dipole calibration comes from the set of revolutions immediately after the Jupiter calibration.

ter calibration and the internal calibrator transfer for the data analysis of this flight of BOOMERANG.

6.4. *In-Flight Noise*

In-flight noise performance is measured computing the power spectrum of the bolometers' signals after despiking and deconvolution, avoiding data taken when the gondola inverts the scanning direction (turnarounds). Noise equivalent temperatures (NETs) are calculated using in-flight calibration constants. In-flight noise includes bolometer noise, electronics noise, signal from the atmosphere, radio frequency noise, signal from the Galaxy, and signal from the CMB. Results are in Table 9. Power spectra are reported in Figure 21 for the channels used in the analysis.

7. SENSITIVITY AND DATA ANALYSIS

The sensitivity of a receiver to fluctuations in sky brightness at different angular scales can be represented by a window function. The shape of the window function depends on the details of the measurement. Calculations have been made for the window functions of different experiments (e.g., White et al. 1994) taking into account different beam shapes and sizes, chopping strategies, signal-processing electronics, and data analysis strategies. Because of the complex chopping strategies employed to obtain stable offsets in these experiments, the window functions are often complicated. Recent experiments attempt to use specially tailored filters to generate multiple well-defined window functions from a single chop (Big Plate, Medium-Scale Anisotropy Measurements). In addition, upcoming space missions will attempt to make fully reconstructed maps of diffuse millimeter-wave emission (*Microwave Anisotropy Probe*, *Planck*). For all of these experiments, the scan strategy is driven by the achievable bandwidth of the detectors, which limits the maximum and minimum scan speed.

In BOOMERANG we have designed our scan strategy and beam size to utilize the full bandwidth and sensitivity of our detectors. The scan speed for both flights of BOOMER-

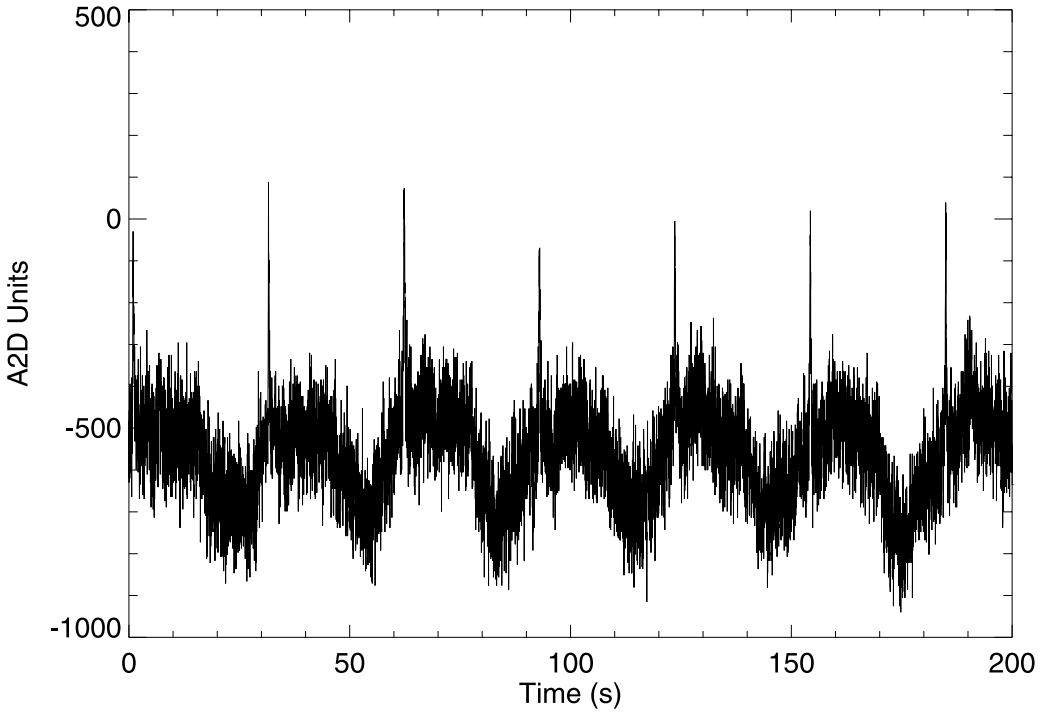

FIG. 18.—Raw data of a fast rotation. The CMB dipole produces a sinusoidal signal. The spike at regular phase is the signal from Jupiter used for time constant measurements. Full rotations of the payload have been repeated 4 times during the flight, at intervals of more than 1 hr.

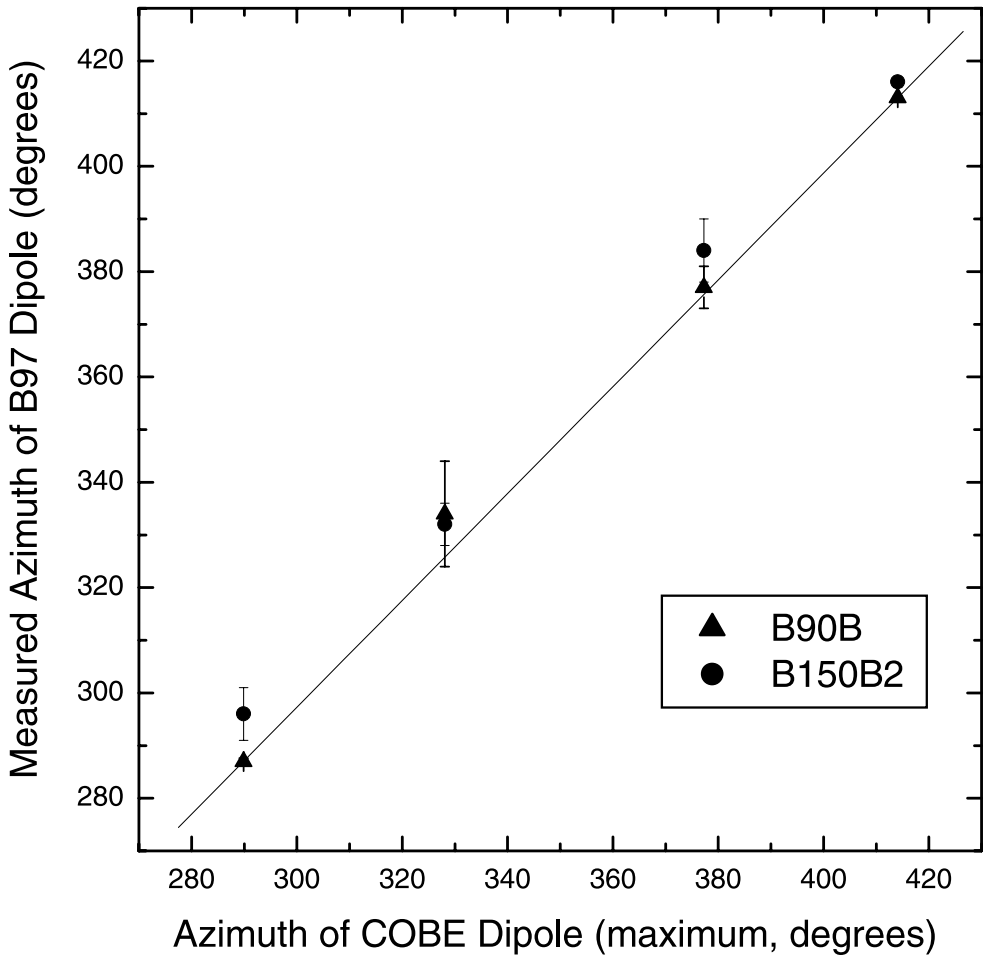

FIG. 19.—Azimuth of the maximum signal vs. azimuth of the expected dipole direction during fast rotations. The good correlation is proof that the signal is originated by the CMB dipole and is not a local effect.

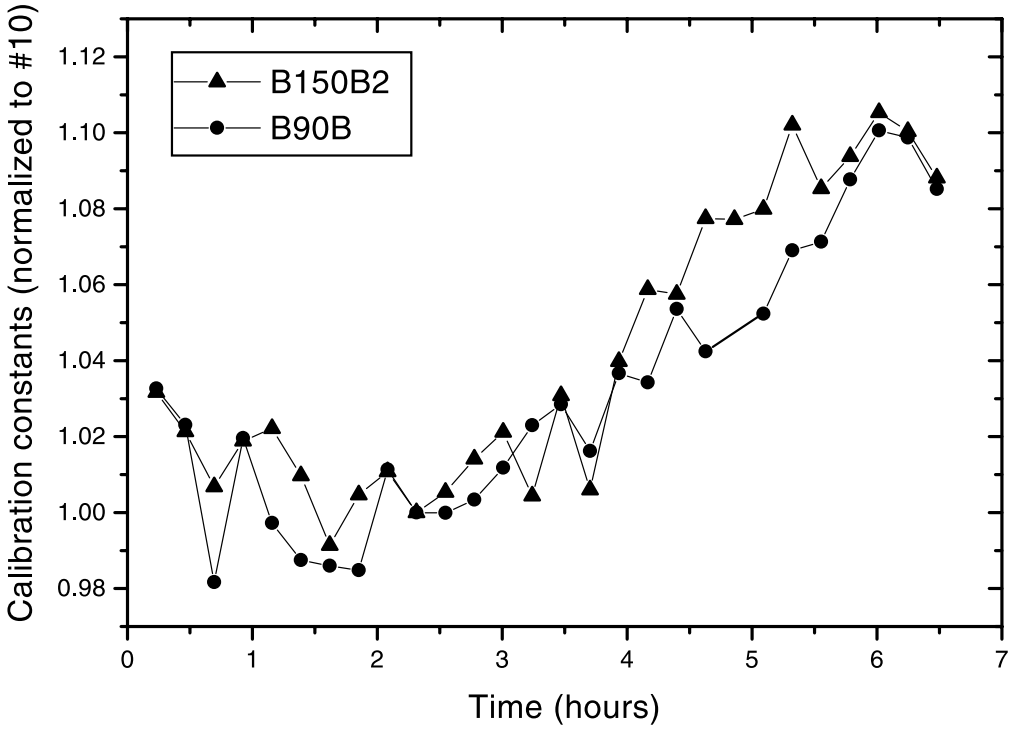

FIG. 20.—Fractional responsivity variations during the flight as measured from the internal calibrator signals, for both channels used in the analysis. Starting from the second hour of flight, the variations are less than 10%. The first 2 hr are not used in the data analysis.

TABLE 9
NOISE EQUIVALENT TEMPERATURE MEASURED IN FLIGHT

Channel	NET_{CMB} ($\mu K\ Hz^{-1/2}$)
NA-B150A1.....	700
NA-B150B1	1000
NA-B150B2	500
NA-B90A	1000
NA-B90B.....	740

ANG is matched to the signal bandwidth of the detectors, and the sensitivity to large angular scales is limited by the stability of the readout electronics and atmospheric fluctuations. BOOMERANG can operate in either total power mode, with the data from each detector analyzed independently, or in chopped mode, differencing between symmetric pixels in the focal plane to remove common mode noise sources. In total power mode, the window function of each channel is limited only by the beam size and the scan length. In differenced mode, the window function is determined by the beam size and beam separation in the focal plane.

The data from the BNA flight have been analyzed as a pixelized map with an experimentally determined correlation matrix describing the noise.

Maps of the B150B2 and B90B channels are in Figure 22. The ~25,000 pixel maps are noise dominated. These maps are produced just by filtering the time-ordered data and co-adding the data in pixels with the HEALPix scheme.[11] The map produced to compute the anisotropies' power spectrum was made using the MADCAP software package.[12] The noise correlation function is estimated from the time-ordered data assumed to be noise dominated.

This analysis, described in Mauskopf et al. (2000), led to an error in the power spectrum measurements of $\sim\pm 15\ \mu K$ at 68% confidence level for band powers averaged over $\Delta\ell = 50$ bins, centered at six multipoles covering the range $25 < \ell < 325$.

8. CONCLUSIONS

The feasibility of extended (many hundred square degree), resolved (20′ FWHM), sensitive CMB maps using quasi–total power balloon-borne microwave photometers has been demonstrated with the BOOMERANG/NA instrument. Critical technologies have been developed in several areas: spider web bolometers, total power readout electronics, low sidelobe response telescope, long-duration cryogenics, and a scan-oriented attitude control system.

The BOOMERANG/LDB (B. P. Crill et al. 2002, in preparation) payload makes optimal use of the technologies described here providing high S/N maps (de Bernardis et al. 2000; Netterfied et al. 2002) of a wide portion of the microwave sky and constraining values of the cosmological parameters (Lange et al. 2001; de Bernardis et al. 2002).

[11] See http://www.eso.org/kgorski/healpix.

[12] See http://www.nersc.gov/~borrill/cmb/madcap.html..

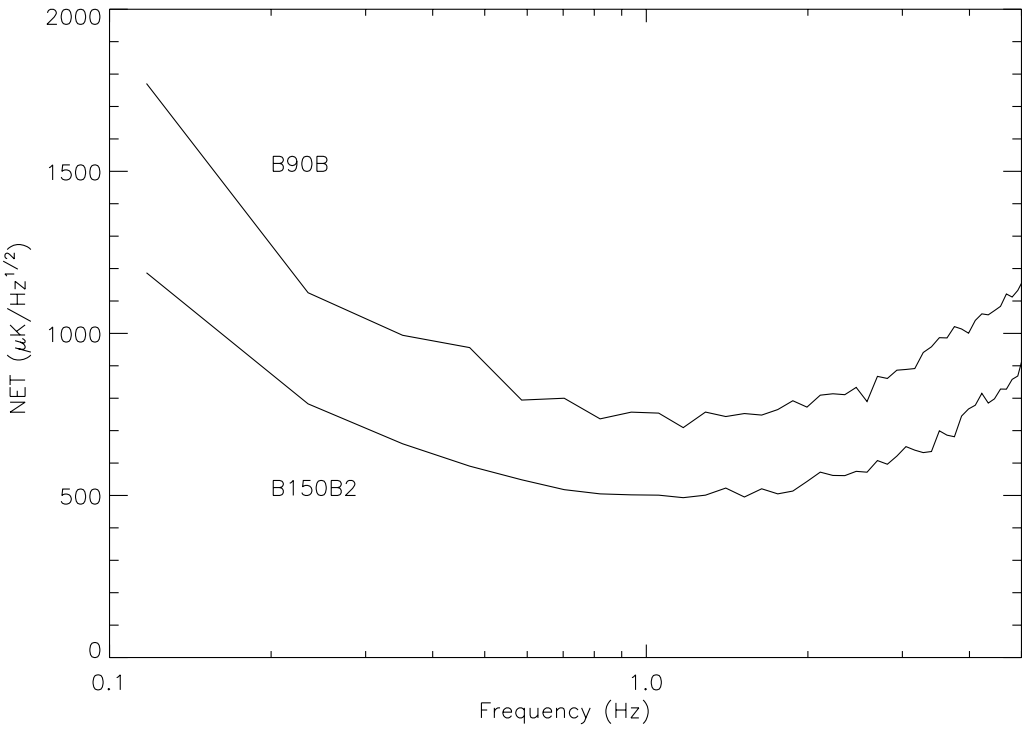

FIG. 21.—Noise equivalent temperature vs. frequency for the two channels used in the analysis of the angular power spectrum of the CMB. At low frequencies 1/f noise dominates. The rise at high frequencies is due to the bolometer time constants: the receiver loses sensitivity and the NET is increased after deconvolution. The most interesting frequencies are around 1.5 Hz, where the first peak of the anisotropies in the CMB is expected to be (with scan speed of $2^\circ\ s^{-1}$ at an elevation of 41°).

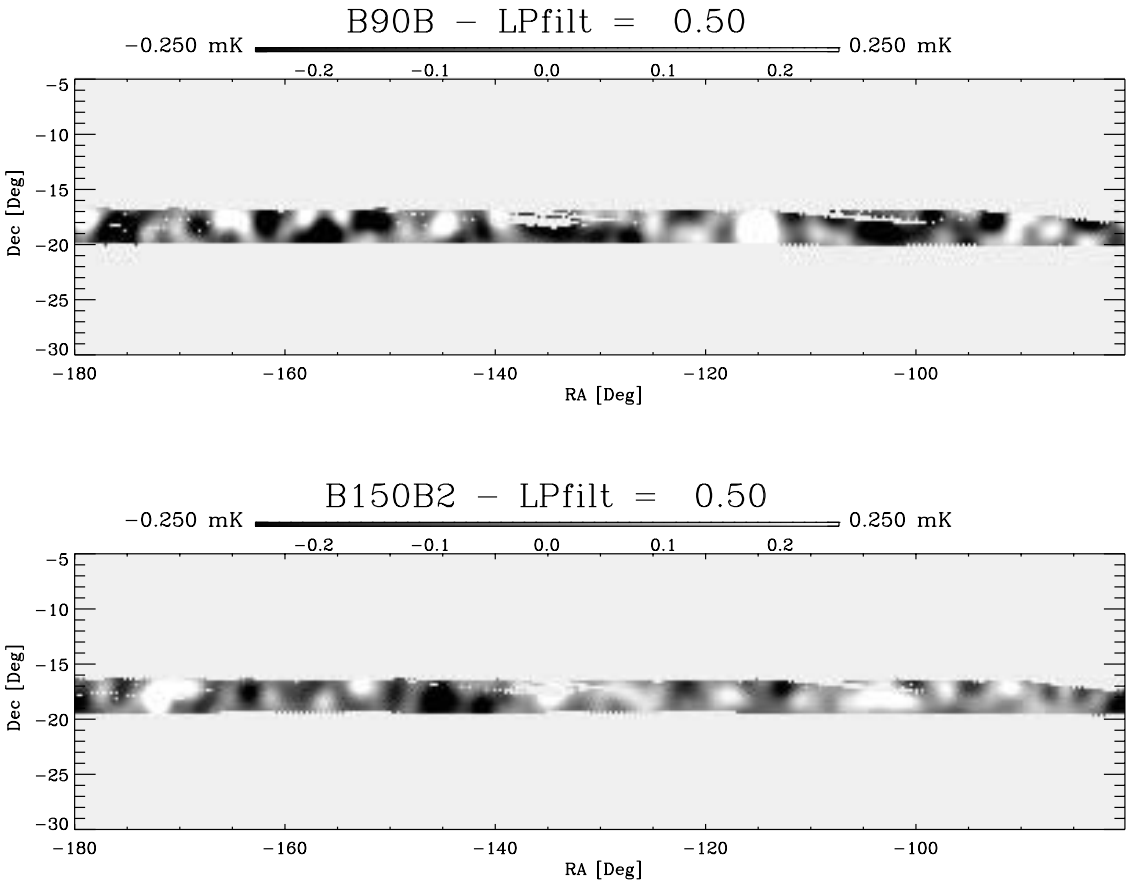

FIG. 22.—Maps of the measured flight from B150B2 and the B90B channels. Both maps are smoothed with a 0°.5 FWHM Gaussian in order to increase the S/N. The structures in the maps are only partially concordant, showing that these maps are noise dominated rather than signal dominated. For better visualization only a portion of the full map (see coverage in Fig. 12) is shown here.

The BOOMERANG experiment has been supported by Programma Nazionale di Ricerche in Antartide, Università di Roma "La Sapienza," and Agenzia Spaziale Italiana in Italy, by NSF and NASA in the US, and by PPARC in the UK. DOE/NERSC provided the supercomputing facilities. We acknowledge the use of HEALPix.

REFERENCES

Alsop, D. C., Inman, C., Lange, A. E., & Wilbanks, T. 1992, Appl. Opt., 31, 6610
Bock, J. J., et al. 1996, in Proc. 30th ESLAB Symp., Submillimetre and Far-Infrared Space Instrumentation, ed. E. J. Rolfe (ESA SP-388; Noordwijk: ESA), 119
Bond, J. R., Crittenden, R., Davis, R. L., Efstathiou, G., & Steinhardt, P. J. 1994, Phys. Rev. Lett., 72, 13
Church, S. E., Ganga, K. M., Holzapfel, W. L., Ade, P. A. R., Mauskopf, P. D., Wilbanks, T. M., & Lange A. E. 1997, ApJ, 484, 523
de Bernardis, P., DeTroia, G., & Miglio, L. 1999, NewA Rev., 43, 281
de Bernardis, P., et al. 1993, A&A, 271, 683
———. 2000, Nature, 404, 955
———. 2002, ApJ, 564, 559
Devlin, M. J., et al. 1994, ApJ, 433, L57
Fixsen, D. J., et al. 1994, ApJ, 420, 445
Goldin, A. B., et al. 1997, ApJ, 488, L161
Haller, E. E., et al. 1994, Proc. SPIE, 2198, 630
Halpern, M., Gush, H. P., Wishnow, E., & De Cosmo, V. 1986, Appl. Opt., 25, 565
Hu, W., Sugiyama, N., & Silk, J. 1997, Nature, 386, 37
Jaffe, A., et al. 2001, Phys. Rev. Lett., 86, 3475
Kogut, A., et al. 1993, ApJ, 419, 1
Lange, A. E., et al. 2001, Phys. Rev. D, 63, 4
Lee, A. T., et al. 1999, in AIP Conf. Proc. 476, 3K Cosmology, ed. L. Maiani, F. Melchiorri, & N. Vittorio (Woodbury: AIP), 224
Masi, S., Aquilini, E., Cardoni, P., de Bernardis, P., Martinis, L., Scaramuzzi, F., & Sforna, D. 1998, Cryogenics, 38, 319
Masi, S., Cardoni, P., de Bernardis, P., Piacentini, F., Raccanelli, A., & Scaramuzzi, F. 1999, Cryogenics, 39, 217
Mauskopf, P., et al. 2000, ApJ, 536, L59
———. 1997, Appl. Opt., 36, 765
Melchiorri, A., et al. 2000, ApJ, 536, L63
Netterfield, C. B., et al. 2002, ApJ, submitted (astro-ph/0104460)
Page, L. A., Cheng, E. S., & Myers, S. S. 1990, ApJ, 355, L1
Pryke, C., et al. 2002, ApJ, in press (astro-ph/0104490)
Smoot, G. F., et al. 1991, ApJ, 371, L1
———. 1992, ApJ, 396, L1
Tanaka, S. T., et al. 1996, ApJ, 468, L81
Ulich, B. L. 1981, AJ, 86, 1619
White, M., Scott, D., & Silk, J. 1994, ARA&A, 32, 319
Wilbanks, T., Devlin, M., Lange, A. E., Sato, S., Beeman, J. W., & Haller, E. E. 1990, IEEE Trans. Nucl. Sci., 37, 566